Gondwana Research 27 (2015) 1494–1508

Contents lists available at ScienceDirect

Gondwana Research

journal homepage: www.elsevier.com/locate/gr

Late Triassic granitic magmatism in the Eastern Qiangtang, Eastern Tibetan Plateau: Geochronology, petrogenesis and implications for the tectonic evolution of the Paleo-Tethys

Touping Peng [a,*], Guochun Zhao [b], Weiming Fan [a], Bingxia Peng [a], Yongsheng Mao [a,c]

[a] State Key Laboratory of Isotope Geochemistry, Guangzhou Institute of Geochemistry, Chinese Academy of Sciences, Guangzhou 510640, China
[b] Department of Earth Sciences, The University of Hong Kong, Pokfulam Road, Hong Kong
[c] Graduate University of Chinese Academy of Sciences, Beijing 100049, China

ARTICLE INFO

Article history:
Received 18 September 2013
Received in revised form 29 December 2013
Accepted 2 January 2014
Available online 8 February 2014

Handling Editor: Z.M. Zhang

Keywords:
Dongdashan batholith
Eastern Tibetan Plateau
Granite
Post-collisional magmatism
Paleo-Tethys

ABSTRACT

Triassic granites are widely exposed in the central Qiangtang, northern Tibetan Plateau. They, therefore, made an important contribution to the growth of the Tibetan Plateau. In this paper, we present zircon U–Pb dating and Hf isotopic results, and whole-rock elemental and Sr–Nd isotopic analyses of the Dongdashan (DDS) batholith in the central Qiangtang in order to understand their petrogenesis and tectonic setting. LA-MC-ICP-MS zircon U–Pb results show that the DDS batholith was emplaced at 220.3 ± 0.7 Ma. All the granites in the DDS possess high A/CNK values (>1.0) and display peraluminous characteristics, similar to S-type granite. Their strongly fractionated REE patterns ($(La/Yb)_N$ = 6.98–13.9) with conspicuous negative Eu anomalies (Eu^*/Eu = 0.51–0.67), together with negative $\varepsilon_{Nd}(t)$ and $\varepsilon_{Nd}(t)$ values, and depleted Nd and Hf model ages, suggest that the DDS granitic magma had a dominantly crustal source, likely the Paleoproterozoic basement (i.e., the Ningduo and Caoqu group metasediments) in the area.

In combination with regional studies, our new geochemical data and geochronological results demonstrate that the Late Triassic magmatism was generated in a post-collisional tectonic setting. The spatial distribution pattern of the Mesozoic igneous rocks, coupled with the exhumation of high-pressure metamorphic rocks in the central Qiangtang, favors a slab breakoff model, which resulted in post-collisional extension and asthenospheric upwelling that induced large-scale partial melting of the middle-lower crust to produce voluminous amounts of felsic magma. Therefore, the occurrence of the Late Triassic post-collisional magmatism, and particularly the exhumation of high-pressure eclogites and blueschists as well as their presence in the lowermost portion of the Late Triassic volcanoclastics in the Qiangtang basin, clearly indicate that the final closure of the of Paleo-Tethys Ocean and associated continent–continent collision between the Gondwana-derived Western Qiangtang and Eastern Qiangtang terranes had not been completed until the early mid-Triassic.

1. Introduction

Granitoids are the important component of the upper crust, and are found in all plate tectonic environments, especially orogenic settings. Their magmas may be derived from different source regions, producing distinct granitoid types (e.g., Chappell and White, 1974; Sylvester, 1989; Eby, 1992; Moyen et al., 2001), such as S-, I- and A-type granites. Accordingly, they provide petrogenetic 'windows' into the evolution of deeper crustal sources, as well as clues to the overall tectonic setting (e.g., Pitcher, 1983; Pearce et al., 1984; Condie and Kröner, 2013). Moreover, different types of granitoid magmatism usually take place in different tectonic regimes during the evolution of orogeny, including subduction, and syn- to post-collisional and post-orogenic extensional settings (e.g., Chappell and White, 1974; Sylvester, 1989; Chappell and White, 1992; Brown, 1994; Barbarin, 1999; Bonin, 2007). For example, many peralkaline and alkaline granites are associated with post-tectonic within-plate extension (e.g., Bonin, 2007), whereas subduction-related granites tend to be metaluminous, although some metaluminous granites are collision-related (e.g., Martin, 1987; Wedepohl, 1991). In addition, granites related to continent–continent collision tend to be peraluminous (e.g., Wedepohl, 1991; Chappell and White, 1992, 2001). However, several studies have demonstrated that the majority of collision-related, strongly peraluminous granites were emplaced in post-collisional settings after the peak of crustal thickening (e.g., Sylvester, 1998). Furthermore, the resultant magmas could have involved the melt and heat input from mantle (Sylvester, 1998; Wang et al., 2010; Peng et al., 2013). In fact, an increasing number of studies have revealed that crustal anatexis during syn-collisional or syn-orogenic settings generally produces leucogranites, which are peraluminous, such as those along the Alpine-Himalayan

* Corresponding author at: Guangzhou Institute of Geochemistry, Chinese Academy of Sciences, P.O. Box 1131, Guangzhou 510640, People's Republic of China. Tel.: +86 20 85292410; fax: +86 20 85291510.
E-mail address: tppeng08@126.com (T. Peng).

1342-937X/$ – see front matter
http://dx.doi.org/10.1016/j.gr.2014.01.009

Mountain chain (e.g., Harrison et al., 1998; Ciancaleoni and Marquer, 2004; Gaillard et al., 2004).

The Qiangtang block lies to the north of the Lhasa terrane and is the most important part of the Tibetan Plateau (Fig. 1a). The discovery of an early Mesozoic high-pressure (HP) to ultrahigh-pressure (UHP) metamorphic belt in the central Qiangtang (Li et al., 2006; Pullen et al., 2008; Liu et al., 2011; Zhai et al., 2011) and the recent identification of the Carboniferous oceanic ophiolites (Zhai et al., 2013c) indicate that the Paleo-Tethys Ocean was most likely situated between the Eastern and Western Qiantang terranes during the late Paleozoic, and its subduction and final closure led to collision between the two terranes (Li and Zheng, 1993; Yang et al., 2011; Zhai et al., 2011, 2013a). It is quite noticeable that the tectono-magmatism related to the evolution of the Paleo-Tethys Ocean made an important contribution to the growth of the Tibetan Plateau. In recent years, many studies have been carried out in this belt in order to decipher the evolution of the Paleo-Tethys Ocean, especially the correlation between the magmatism, metamorphism and sedimentation, and the tectonic regime transition from subduction to collision in the area (e.g., Pullen et al., 2008; Liu et al., 2011; Yang et al., 2011; Zhai et al., 2011, 2013a). Nonetheless, the tectonic setting of the middle–late Triassic tectono-magmatism, especially for the late Triassic magmatism and sedimentation in the Qiangtang block, is still an issue of debate (Wang et al., 2008; Fu et al., 2010; Zhai et al., 2011, 2013a). Hence, knowledge about the syn- to post-collisional history in this region remains unknown. Moreover, in the case of the granite belt that is parallel to the HP metamorphic belt in the central Qiangtang, little attention has been paid to its association with the middle–late Triassic volcanoclastic and metamorphic rocks (Kapp et al., 2000, 2003). The significance of these granites in a reconstruction of the Paleo-Tethys remains uncertain, because few geochronological and geochemical data are available.

In this contribution, we present whole-rock geochemical and Sr–Nd isotopic compositions, and zircon U–Pb dating and Lu–Hf isotope results for the Late Triassic granites in the central Qiangtang, Eastern Tibetan Plateau. Based on our data, coupled with regional results, our aims are to: (1) illustrate the nature and source of the protoliths of the Late Triassic granites and their melting process; (2) shed insights into the geodynamic mechanism of their generation; and 3) discuss the relationships between the Late Triassic crustal anatexis and the evolution of the Paleo-Tethys.

2. Geological background and petrography

The Eastern Tibetan Plateau is a collage of several blocks or microplates (terranes), including the Songpan–Ganzi, Yidun, Qiangtang and Eastern Lhasa terranes, where numerous important geological records related to the evolution of the Eastern Paleo-Tethys have been well documented (Lv et al., 1993; Pan et al., 2003; Zhang and Santosh, 2012; Zhang et al., 2012; Zheng et al., 2013; Zhu et al., 2013; Zhang et al., in 2014). It is also a key metallogenic district, named as the Tethys metallogenic domain in West China (Pan et al., 2003; Hou et al., 2011; Wang et al., 2014; and references therein), in which many economically important Cu-polymetallic ore deposits have been discovered, such as the Yulong, Zhongdian, Yangla and Narigongma porphyry Cu ore deposits (Hou et al., 2007; Liang et al., 2009; Wang et al., 2011; Yang

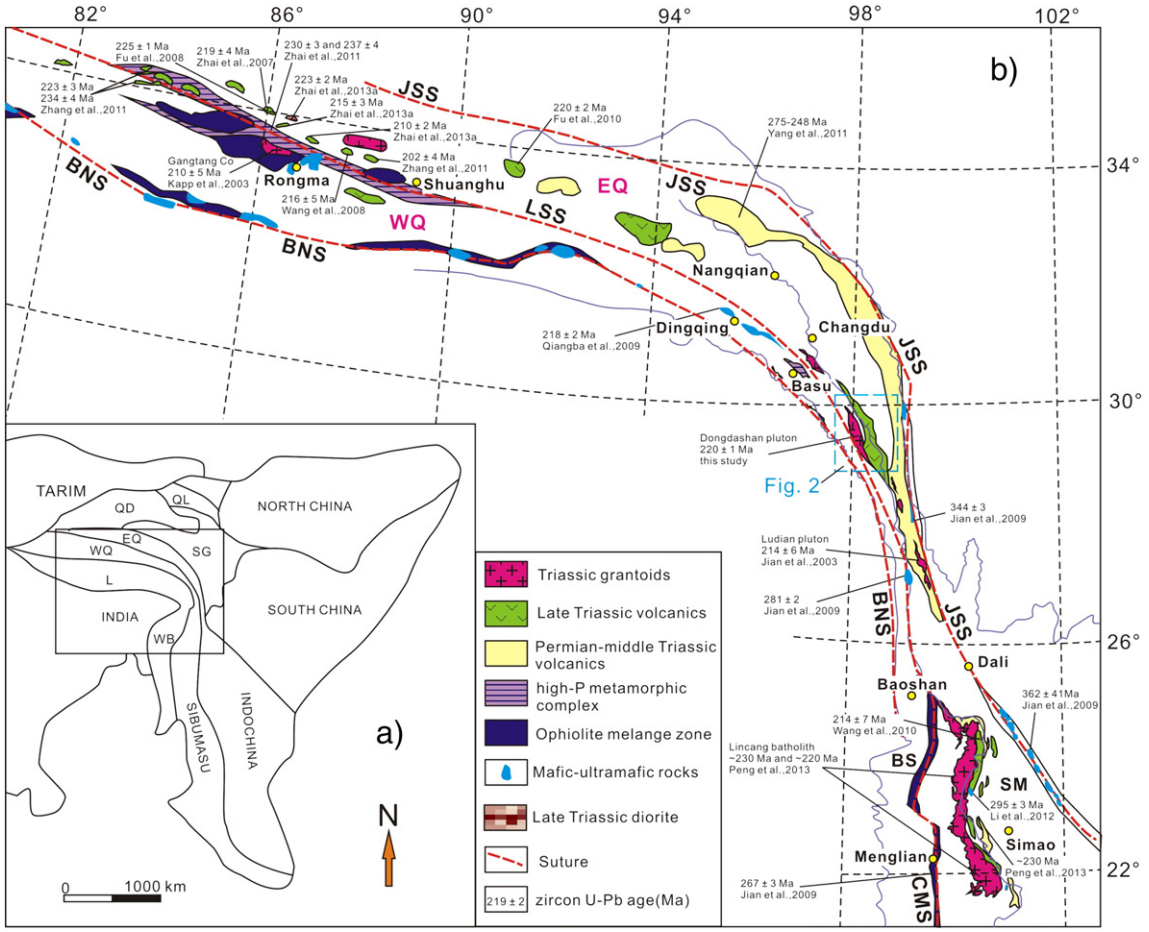

Fig. 1. Simplified geological map (a) and tectonic units (b) of the Sanjiang region in eastern Tibet and Yunnan, SW China (modified from Liu et al., 2011; Deng et al., 2012; Metcalfe, 2013). Tectonic sutures: *BNS*, Bangong–Nujiang suture; *CMS*, Changling–Menglian suture; *JSS*, Jinshajiang suture; *LSS*, Longmu Co–Shuanghu suture. Continental blocks: *BS*, Baoshan; *EQ*, Eastern Qiangtang; *L*, Lhasa; *QD*, Qaidam; *QL*, Qilian; *SG*, Songpan Ganzi; *SM*, Simao; *WB*, West Burma; *WQ*, Westernern Qiangtang. Available ages (with references) are included.

et al., 2012), and the Gachun and Luchun volcanogenic massive sulfide (VMS) ore deposits (Wang et al., 2001; Hou et al., 2003; Pan et al., 2003).

The Qiangtang block lies in the north-central Tibetan plateau (Fig. 1a). It is separated from the Songpan–Ganzi terrane to the east by the Jinsha suture that represents the back-arc basin of the Paleo-Tethys, and from the Lhasa block to the west by the Bangong–Nujiang Mesotethyan suture (Fig. 1a; XZBGM, 1993). The only dated basement rocks in the Qiangtang block are orthogneisses from the Duguer Shan (476–474 Ma; Pullen et al., 2011) and a block of mafic gneiss in mélange near Gangma Co that yielded Cambrian and Ordovician zircon ages (Kapp et al., 2000). Based on the significant distinction in the strata, fossil assemblages and paleomagnetic data before the later Middle Permian (XZBGM, 1993; Li and Zheng, 1993; Zhang et al., 2010), the Qiangtang block can be subdivided into two parts: the Eastern Qiangtang (also termed Qamdo or Changdu) and Western Qiangtang terranes, of which the former is dominantly covered by Upper Triassic–Upper Jurassic intercalated marine siliciclastic rocks and limestones, with Carboniferous–Permian shelf sediments at its easternmost and western margins (Li and Zheng, 1993; XZBGM, 1993; Zhang et al., 2002; Pan et al., 2004; Li et al., 2006; Zhang et al., 2006c), which shows a Gondwana affinity (Zhu et al., 2011; Metcalfe, 2013). In contrast, the Western Qiangtang block consists of Carboniferous–Permian shelf strata along with Jurassic marine rocks on its northern and southern margins, which has a Cathaysian affinity, similar to the Southern China Block (Fig. 1b; Li and Zheng, 1993; XZBGM, 1993; Zhang et al., 2002; Pan et al., 2004; Li et al., 2006; Zhang et al., 2006c). The two terranes are separated by the Early Triassic HP–UHP metamorphic belt, also named as the Central Qiangtang metamorphic belt: QMB (Kapp et al., 2003; Li et al., 2006; Zhang et al., 2006a,b; Pullen et al., 2008) that is composed of blueschist, eclogite, ophiolitic mélange, and metasedimentary rocks (including greenschist, glaucophane-bearing marble and minor chert) (Li and Zheng, 1993; XZBGM, 1993; Kapp et al., 2000, 2003; Li et al., 2006; Zhang et al., 2006a,b; Zhai et al., 2011). The QMB extends from west (Longmu Co area) to east (Shuanghu area) over a distance of ~500 km (Fig. 1b; Li and Zheng, 1993; Li et al., 2006; Zhang et al., 2006a,b), and likely links southeastward with the Ando–Basu HP metamorphic belt (AMB) (Fig. 1a; Zhang et al., 2008; Zhang and Tang, 2009; Zhang et al., 2010), because they have similar basement and deformation histories (Zhang and Tang, 2009; Zhang et al., 2014). Radioactive isotopic dating and P–T estimation of the metamorphic rocks revealed that they had experienced HP–UHP metamorphism at ~244 Ma (Pullen et al., 2008) and subsequent retrograde processes from ~237 Ma to 202 Ma (Kapp et al., 2000, 2003; Zhai et al., 2011).

Recently, some typical ophiolitic lithological assemblages of metamorphosed ultramafic rocks, gabbro cumulates, diabases, pillow basalts, and radiolarian cherts along the southern part of the Eastern Qiangtang block, north of the Longmu Co-Shuanghu suture, have also been recognized (Zhai et al., 2007; Zhai et al., 2011). Zircon U–Pb dating of cumulate gabbros and plagiogranites demonstrated that these oceanic slices formed mainly at 438–348 Ma (Shi et al., 2009; Yang et al., 2011), indicating that the Paleo-Tethys Ocean had developed at least since the Early Silurian. Also, some subduction-related arc magmatic rocks, including andesites, rhyodacites and granites, have been recognized along the southern part of the Eastern Qiangtang (Yang et al., 2011). Zircon U–Pb ages (275–248 Ma) revealed that oceanic/continental subduction in the area might have lasted until the Early Triassic (Yang et al., 2011). Most recently, a large number of Early Permian (~280 Ma) mafic dyke swarms were discovered in the QMB, although they were thought to be the products of a Large Igneous Province (LIP) (Zhai et al., 2013b).

In addition, an important feature is that the Late Triassic magmatism is extensive across the central Qiangtang, particularly in the Mesozoic Qiangtang basin (XZBGM, 1993; Wang et al., 2007; Zhai and Li, 2007). These igneous rocks form a huge Late Triassic magmatic zone, including a large volume of volcanic rocks in the Mesozoic Qiangtang basin and a granitic belt, parallel to the Longmu Co–Shuanghu suture (Fig. 1b). The Late Triassic volcanic rocks are dominated by dacite, rhyolite, felsic tuff and volcanic breccia, with minor andesites and basaltic rocks (XZBGM, 1993; Wang et al., 2007; Zhai and Li, 2007). In composition, they display a bimodal affinity (Zhai et al., 2011; Zhang et al., 2011). Furthermore, some volcanic rocks, as well as diorites, geochemically resemble adakites or adakitic rocks (Zhai et al., 2011). At present, numerous studies have been concentrated on their petrogenesis and rock-forming tectonic setting, and different models have been proposed (e.g., Fu et al., 2010; Zhai et al., 2011, 2013a).

Numerous granitic intrusions occur along the Longmu Co–Shuanghu suture and extend southwards into the Amdo area, forming a granitic belt that stretches from west to east over a length of 1000 km (Fig. 1b). Three relatively large granitic bodies with an exposure of >1000 km^2 include the Rongma intrusion in the westernmost portion and the Jitang and Dongdashan (DDS) intrusions in the easternmost segment (Fig. 1b). The DDS batholith intruded the Early Carboniferous Kagong Group (C_1kg) (Fig. 2). The Kagong Group consists of two formations, including slates and metasandstones with minor interlayered marbles, in the lower section, and marbles and slates with minor interbedded metasandstones, in the upper section (XZBGM, 1993). These granitic intrusions are not deformed and metamorphosed.

3. Sampling and analytical techniques

3.1. Sampling

In this study, we collected one granitic sample from the DDS intrusion for LA-MC-ICP-MS zircon U–Pb dating (Fig. 2). The sample for zircon dating (11ST-60F) was collected from the Mangkang–Zuogong road (N29°43.663, E97°58.354; Fig. 2) in the central part of the Dongdashan batholith; other five samples (11ST-60A, 11ST-60C, 11ST-60E, 11ST-61A and 11ST-60C) were collected along the Mangkang–Zuogong road, for chemical analysis. All studied samples have not undergone any deformation or metamorphism. They are coarse-grained and massive with minor microgranular enclaves. The granites are composed of K-feldspar (~25–35 vol.%), plagioclase (~27–36 vol.%), quartz (~16–32 vol.%), biotite (~8–12 vol.%), with minor zircon, apatite, titanite and iron oxides. Based on modal mineral compositions obtained by point counting and then plotting on a QAP diagram (Fig. 3), all the samples plot within the monzogranite field.

3.2. Zircon U–Pb analysis

Zircons for LA-MC-ICP-MS U–Pb dating were separated from sample 11ST-60F by using conventional heavy liquid and magnetic techniques and purified by handpicking under a binocular microscope. The zircon grains were mounted in epoxy resin, polished to half their thickness, and gold coated, and then photographed in transmitted and reflected light. The internal structure of zircons was examined using cathodoluminescence (CL) imaging prior to U–Pb isotopic analysis. The CL images were obtained using an EMPA-JXA-8100 scanning electron microscope at the Guangzhou Institute of Geochemistry, Chinese Academy of Sciences, Guangzhou. Zircon U–Pb isotopes were analyzed by LA-MC-ICP-MS at the Department of Earth Sciences, the University of Hong Kong, using a Nu Plasma HR MC-ICP-MS, equipped with a 193 nm excimer laser ablation system (Resolution M-50) using a ~5 J/cm^2 energy density, 6 Hz laser cycle and 30 μm beam diameter. The detailed analytical methods follow those of Xia et al. (2011). U–Pb raw data were corrected offline using ICPMSDataCal 7.0 (Liu et al., 2010) with zircon 91500 as the external standard. All ages were plotted using the Isoplot 3.23 program (Ludwig, 2003) and the results were reported with 1σ errors. To quantitatively supplement the visual comparisons of binned frequency histograms from detrital zircon ages from two samples, the K–S statistics was used to compare their cumulative probability plots (Press et al., 1986). The K–S test determines a

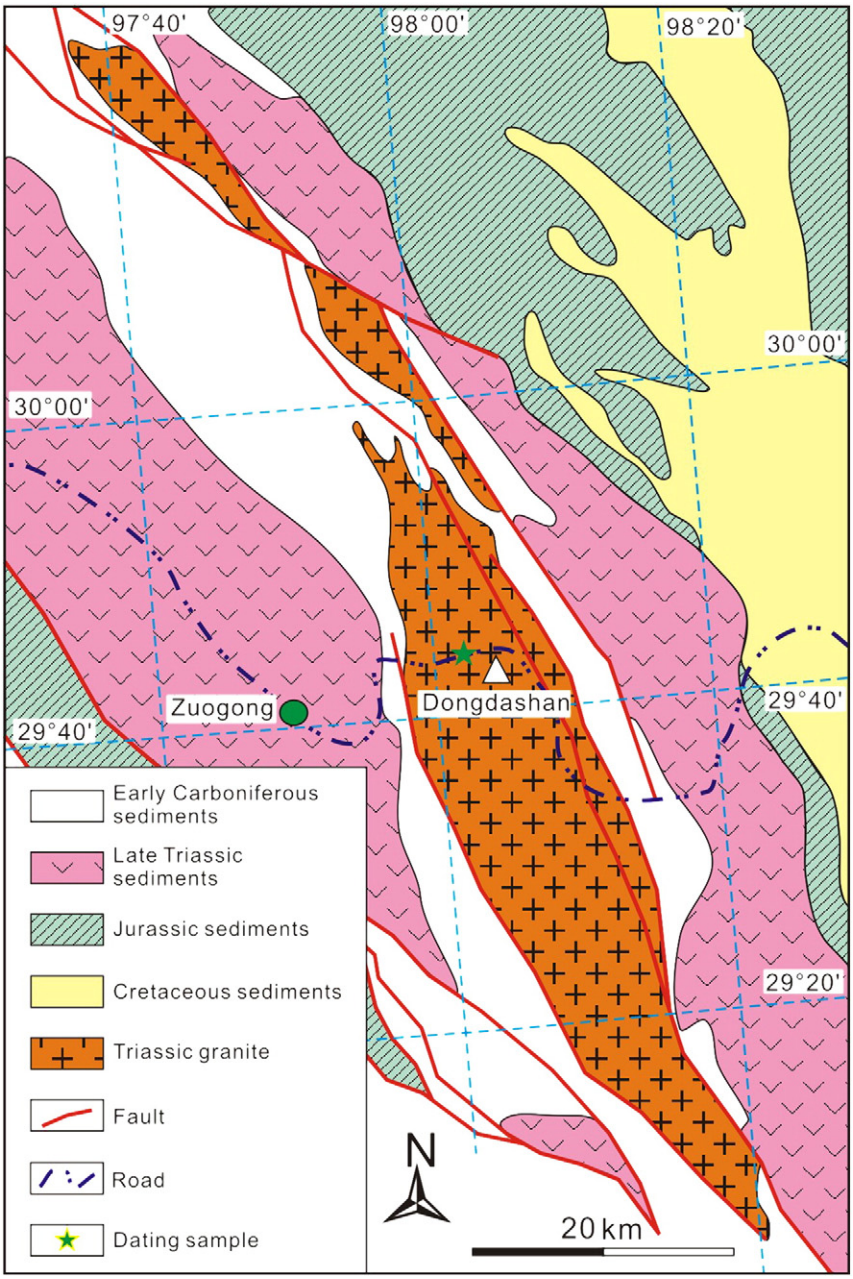

Fig. 2. Geological map of the Dongdashan area.
Modified after Pan et al., 2004.

probability (P) that assesses whether differences between two cumulative probability plots could be due to random choice of grains during analysis. If $P > 0.05$, there is 95% confidence that two cumulative probability plots reflect statistically indistinguishable zircon sources. Common Pb was corrected according to the method proposed by Anderson (2002). The U–Pb ages were calculated using the U decay constants of Steiger and Jäger (1997) and Isoplot Ex 3 software (Ludwig, 2003). Individual analyses are presented with 1σ error (95% confidence level). U–Pb zircon results are listed in Table 1, and their U–Pb concordia plots and representative zircon CL images are shown in Fig. 4.

3.3. Zircon Hf isotope analysis

Analytical methods for zircon Hf isotope analysis were described in detail in Xia et al. (2011) and are summarized below. Analyses were carried out in situ with the laser-ablation system Resolution M-50, attached to a Nu Plasma HR MC-ICP-MS, at the University of Hong Kong. All analyses were obtained using a beam diameter of 55 μm and the energy density of 15–20 J/cm^2. Interference of ^{176}Lu on ^{176}Hf was corrected by measuring ^{172}Yb and ^{175}Lu, respectively. In situ calculated ^{173}Yb/^{172}Yb ratio was used for mass bias correction for both Yb and Lu because of their similar physicochemical features. Ratios used for the corrections are 0.5887 of ^{176}Yb/^{172}Yb and 0.02655 of ^{176}Lu/^{175}Lu, respectively. Zircon 91500, with a recommended ^{176}Hf/^{177}Hf ratio of 0.282306 ± 10 (Woodhead et al., 2004), was used as the reference standard afterwards. $\varepsilon_{Hf}(t)$ values were calculated using the measured U–Pb ages and with reference to the chondritic reservoir (CHUR) present-day ^{176}Hf/^{177}Hf = 0.282772 and ^{176}Lu/^{177}Hf = 0.0332 (Blichert-Toft and Albarede, 1997). Single-stage Hf model ages (T_{DM1}(Hf)) were calculated relative to the depleted mantle present-day value of ^{176}Hf/^{177}Hf = 0.28325 and ^{176}Lu/^{177}Hf = 0.0384 (Griffin et al., 2000). We also calculated a 'crustal'

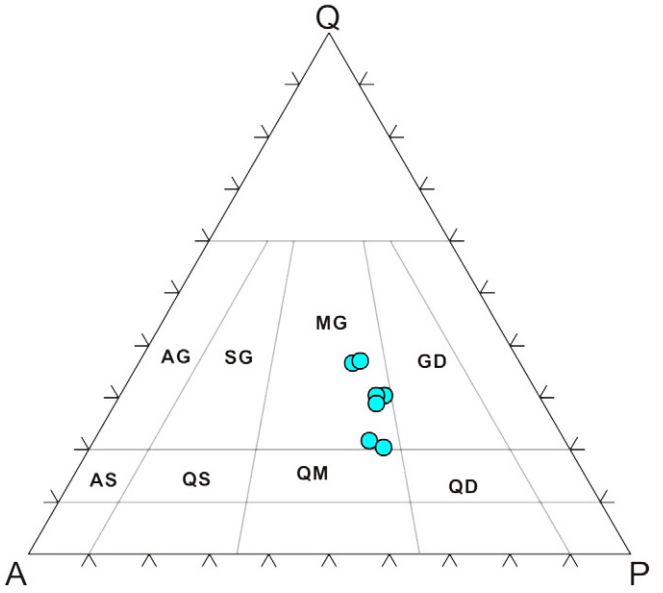

Fig. 3. Modal classification of the granitoids (after Streckeisen, 1967). AG = alkali-feldspar granite; AS = alkali-feldspar syenite; SG = syenogranite; QS = quartz syenite; MG = monzogranite; QM = quartz monzonite; GD = granodiorite; QD = quartz monzodiorite.

model age (T_{DM2}(Hf)), which assumes that the parental magma was produced from average continental crust ($^{176}Lu/^{177}Hf = 0.015$, Griffin et al., 2004) that originally was derived from the depleted mantle. The zircon Hf analyses were obtained using the same mounts as those used for U–Pb dating and data were collected over the U–Pb spots in most cases but, where this is not possible, they were run on adjacent sites within the same CL domain. The analytical results are listed in Table 2.

3.4. Whole-rock major-trace element and Sr–Nd isotope analysis

Major oxide contents were determined at the Guangzhou Institute of Geochemistry, Chinese Academy of Sciences (GIGCAS), Guangzhou, using a wavelength X-ray fluorescence (XRF) spectrometer with analytical errors better than 2%. Trace element analyses were performed at the Institute of Geochemistry, CAS, Guiyang, China, by inductively coupled plasma mass spectrometry (ICP-MS). The detailed analytical protocol is described in Qi et al. (2000). The analytical precision is better than 5% for elements >10 ppm, better than 8% for those <10 ppm, and about 10% for transition metals. The analytical results are presented in Table 3.

Sr and Nd isotopic compositions were measured using a Triton Thermal Ionization Mass Spectrometry (TIMS) and a Micromass Isoprobe multi-collector-inductively coupled plasma-mass spectrometer (MC-ICP-MS) at GIGCAS, respectively. Analytical procedures for Sr and Nd isotopes are described in detail by Li et al. (2004) and Chen et al. (2010). The $^{87}Sr/^{86}Sr$ value of the NBS987 standard and the $^{143}Nd/^{144}Nd$ value of the JNdi-1 standard were 0.710288 ± 28 (2σ) and 0.512109 ± 12 (2σ), respectively; fractionation corrections of $^{146}Nd/^{144}Nd = 0.7219$ and $^{86}Sr/^{88}Sr = 0.1194$ were applied to all measured $^{143}Nd/^{144}Nd$ and $^{86}Sr/^{88}Sr$ values, respectively. The Sr–Nd isotopic analytical results are presented in Table 4.

4. Results

4.1. Zircon U–Pb and Lu–Hf results

Zircons from the monzogranite sample (11ST-60F) from the DDS batholith are dominantly light pink to colorless euhedral crystals. Most grains range in length from 100 to ~300 μm with length/width ratios of 3:1. Zircons exhibit oscillatory magmatic zoning in CL images, although some have inherited cores (Fig. 4b and c).

The analyzed zircons from sample 11ST-60F have an age range from 220.0 to 276.7 Ma, with Th/U ratios ranging from 0.16 to 0.57 (Table 1). All analyzed spots are concordant. The fifteen youngest spots give a weighted mean $^{206}Pb/^{238}U$ age of 220.3 ± 0.7 Ma (MSWD = 0.5; Fig. 4a), which can be interpreted as the crystallization age of the granite. The older ages, including 276.7 ± 3.9 Ma, 254.6 ± 5.6 Ma (weighted mean age), 239.7 ± 1.0 Ma, 236.0 ± 1.3 Ma and 232.6 ± 1.0 Ma (weighted mean age) (Fig. 4a and Table 1), were obtained from cores and xenocrysts. The Permian–Early Triassic ages are consistent with the times of arc magmatism (275–248 Ma) in the area as reported recently by Yang et al. (2011), while the middle Triassic age (240–230 Ma) is well coupled with the zircon dating results from two

Table 1
LA-ICP-MS U-Pb data for zircons from the Late Triassic granite in the Eastern Qiangtang.

Analysis	Th/U	Corrected isotope ratios						Isotope ages (Ma)					
		$^{207}Pb^a/^{206}Pb^a$	±1σ	$^{207}Pb^a/^{235}U$	±1σ	$^{206}Pb^a/^{238}U$	±1σ	$^{207}Pb^a/^{206}Pb^a$	±1σ	$^{207}Pb^a/^{235}U$	±1σ	$^{206}Pb^a/^{238}U$	±1σ
11ST-60F-1	0.37	0.0509	0.0003	0.2441	0.0031	0.0348	0.0004	235.3	11.1	221.8	2.5	220.3	2.4
11ST-60F-2	0.38	0.0510	0.0001	0.2663	0.0012	0.0379	0.0002	239.0	10.2	239.7	1.0	239.7	1.0
11ST-60F-3	0.57	0.0508	0.0003	0.2573	0.0018	0.0367	0.0001	231.6	17.6	232.5	1.5	232.4	0.7
11ST-60F-4	0.53	0.0509	0.0003	0.2616	0.0019	0.0373	0.0002	235.3	17.6	236.0	1.5	236.0	1.3
11ST-60F-5	0.46	0.0506	0.0002	0.2430	0.0015	0.0348	0.0002	220.4	9.3	220.8	1.2	220.8	1.1
11ST-60F-6	0.45	0.0506	0.0001	0.2427	0.0022	0.0348	0.0003	233.4	5.6	220.7	1.8	220.4	1.9
11ST-60F-7	0.42	0.0509	0.0002	0.2588	0.0019	0.0369	0.0002	235.3	11.1	233.7	1.5	233.5	1.2
11ST-60F-8	0.49	0.0510	0.0001	0.2446	0.0013	0.0348	0.0002	239.0	10.2	222.2	1.1	220.4	1.0
11ST-60F-9	0.20	0.0514	0.0003	0.2873	0.0066	0.0405	0.0009	257.5	38.9	256.4	5.2	256.2	5.6
11ST-60F-10	0.52	0.0506	0.0002	0.2427	0.0016	0.0348	0.0002	233.4	7.4	220.6	1.3	220.4	1.4
11ST-60F-11	0.53	0.0506	0.0002	0.2425	0.0025	0.0348	0.0004	220.4	7.4	220.4	2.0	220.4	2.3
11ST-60F-12	0.34	0.0506	0.0001	0.2430	0.0016	0.0348	0.0002	233.4	5.6	220.9	1.3	220.6	1.3
11ST-60F-13	0.50	0.0509	0.0002	0.2574	0.0018	0.0367	0.0002	235.3	11.1	232.6	1.5	232.2	1.0
11ST-60F-14	0.31	0.0505	0.0001	0.2419	0.0012	0.0347	0.0002	220.4	8.3	220.0	1.0	220.0	1.0
11ST-60F-15	0.45	0.0511	0.0002	0.2448	0.0022	0.0347	0.0002	255.6	9.3	222.4	1.8	220.0	1.3
11ST-60F-16	0.36	0.0507	0.0002	0.2430	0.0015	0.0348	0.0002	227.8	7.4	220.8	1.2	220.2	1.2
11ST-60F-17	0.47	0.0505	0.0001	0.2430	0.0028	0.0349	0.0004	220.4	10.2	220.9	2.3	220.9	2.3
11ST-60F-18	0.16	0.0504	0.0001	0.2416	0.0040	0.0348	0.0006	213.0	5.6	219.8	3.2	220.3	3.5
11ST-60F-19	0.23	0.0511	0.0001	0.2450	0.0031	0.0348	0.0004	255.6	5.6	222.5	2.5	220.2	2.6
11ST-60F-20	0.25	0.0513	0.0002	0.2844	0.0039	0.0402	0.0005	253.8	2.8	254.1	3.1	254.1	3.3
11ST-60F-21	0.27	0.0520	0.0005	0.3132	0.0037	0.0439	0.0006	283.4	20.4	276.7	2.9	276.7	3.9
11ST-60F-22	0.28	0.0502	0.0001	0.2409	0.0020	0.0348	0.0003	205.6	7.4	219.1	1.6	220.3	1.6
11ST-60F-23	0.42	0.0505	0.0002	0.2419	0.0011	0.0347	0.0001	220.4	10.2	220.0	0.9	220.0	0.8

a = Radiogenic lead.

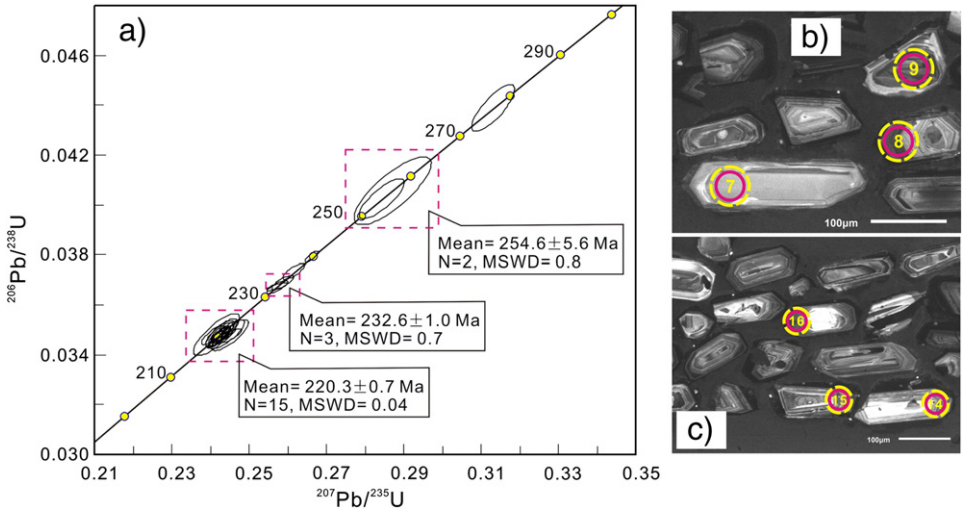

Fig. 4. LA-ICP-MS zircon U–Pb concordia plots for the Dongdashan granite from the central Qiangtang and the representative zircons (some analyzed grains with $^{206}Pb/^{238}U$ age and $\varepsilon_{Hf}(t)$ values). The number in the circle is the analyzed spot.

eclogite samples (230 ± 3 Ma and 237 ± 4 Ma, Zhai et al., 2011). Hence, it is likely that these zircons are xenocrysts entrapped by the granitic magma during their ascent. The calculated zircon saturation temperatures are <800 °C (Table 1). Taking into account the presence of inherited zircons in the granites, it is evident that zirconium was saturated in the magma source. Therefore, T_{Zr} should place an upper limit on magma temperature (Miller et al., 2003).

Twenty three zircon grains from the sample were analyzed for Lu–Hf isotopic composition (Table 2). All analyses of zircons yielded a relatively low $^{176}Hf/^{177}Hf$ ratio between 0.282123 and 0.282398 and a wide range of $\varepsilon_{Hf}(t)$ values from −18.33 to −8.30 (Table 2; Fig. 5) with $T_{DM2}(Hf)$ model ages ranging from 1.79 Ga to 2.41 Ga.

4.2. Major and trace element data

Major and trace element compositions and Sr–Nd isotopic results of all samples are listed in Tables 3 and 4, respectively. The DDS granites have slightly variable major element contents, with SiO_2 = 67.04–67.50 wt.%, MgO = 1.21–2.44 wt.%, CaO = 2.20–3.25 wt.%, Al_2O_3 = 13.98–15.43 wt.%, Fe_2O_3t = 3.95–4.38 wt.% and total alkali ($K_2O + Na_2O$) contents of 5.94 to 6.92 wt.%. These characteristics, together with high K_2O/Na_2O ratios (1.27–1.64), show that most granites belong to the high-K calc-alkaline series (Fig. 6a). They have a range of A/CNK values (mol. $Al_2O_3/(CaO + K_2O + Na_2O)$) of 1.03–1.19, which are >1.0, indicating that they are peraluminous granites (Fig. 6b;

Table 2
Lu–Hf isotopic compositions of zircons from the Late Triassic granite in the eastern Qiangtang.

Analysis	$^{176}Hf/^{177}Hf$	±1σ	$^{176}Lu/^{177}Hf$	$^{176}Yb/^{177}Hf$	$^{207}Pb/^{206}Pb$ age (Ma)	$^{176}Hf/^{177}Hf$ (i)	$\varepsilon_{Hf}(t)$	$T_{DM1}(Hf)$ (Ga)	$T_{DM2}(Hf)$ (Ga)	$f_{Lu/Hf}$
11ST-60F										
60F-1	0.282281	0.000014	0.001005	0.023188	220	0.282277	−12.67	1.37	2.06	−0.97
60F-2	0.282319	0.000014	0.001060	0.026169	240	0.282314	−10.94	1.32	1.96	−0.97
60F-3	0.282261	0.000016	0.001493	0.037520	232	0.282254	−13.21	1.42	2.10	−0.96
60F-4	0.282292	0.000018	0.001366	0.035754	236	0.282286	−12.03	1.37	2.03	−0.96
60F-5	0.282123	0.000018	0.001478	0.038205	221	0.282117	−18.33	1.61	2.41	−0.96
60F-6	0.282319	0.000011	0.001434	0.034004	220	0.282313	−11.41	1.33	1.98	−0.96
60F-7	0.282398	0.000013	0.001194	0.028664	233	0.282393	−8.30	1.21	1.79	−0.96
60F-8	0.282357	0.000013	0.001895	0.049183	220	0.282349	−10.13	1.30	1.90	−0.94
60F-9	0.282256	0.000013	0.001517	0.037501	256	0.282249	−12.88	1.43	2.10	−0.95
60F-10	0.282338	0.000010	0.001194	0.029734	220	0.282333	−10.71	1.30	1.93	−0.96
60F-11	0.282304	0.000018	0.001304	0.032685	220	0.282299	−11.90	1.35	2.01	−0.96
60F-12	0.282287	0.000021	0.001663	0.040814	221	0.282280	−12.57	1.39	2.05	−0.95
60F-13	0.282299	0.000014	0.001415	0.035978	232	0.282293	−11.85	1.36	2.01	−0.96
60F-14	0.282356	0.000010	0.001684	0.039575	220	0.282349	−10.14	1.29	1.90	−0.95
60F-15	0.282380	0.000013	0.001543	0.040759	220	0.282374	−9.25	1.25	1.84	−0.95
60F-16	0.282306	0.000013	0.000904	0.022674	220	0.282302	−11.80	1.33	2.00	−0.97
60F-17	0.282363	0.000021	0.001444	0.034315	221	0.282357	−9.83	1.27	1.88	−0.96
60F-18	0.282375	0.000013	0.000951	0.023109	220	0.282371	−9.36	1.24	1.85	−0.97
60F-19	0.282360	0.000015	0.000951	0.025254	220	0.282356	−9.89	1.26	1.88	−0.97
60F-20	0.282385	0.000012	0.001629	0.041912	254	0.282377	−8.38	1.25	1.81	−0.95
60F-21	0.282312	0.000019	0.001745	0.041515	277	0.282303	−10.50	1.35	1.96	−0.95
60F-22	0.282315	0.000009	0.001243	0.032898	220	0.282310	−11.52	1.33	1.98	−0.96
60F-23	0.282353	0.000008	0.000962	0.023229	220	0.282349	−10.14	1.27	1.90	−0.97

The $^{176}Hf/^{177}Hf$ and $^{176}Lu/^{177}Hf$ ratios of chondrite and depleted mantle at the present day are 0.282772 and 0.0332, and 0.28325 and 0.0384, respectively, Blichert-Toft and Albarede (1997), Griffin et al. (2000). $\lambda = 1.865 \times 10 - 11\ a^{-1}$, Scherer et al. (2001). $(^{176}Lu/^{177}Hf)_c = 0.015$, t = crystallization age of zircon.
$\varepsilon_{Hf}(t) = 10{,}000 \times \{[(^{176}Hf/^{177}Hf)_S - (^{176}Lu/^{177}Hf)_S \times (e^{\lambda t} - 1)] / [(^{176}Hf/^{177}Hf)_{CHUR,0} - (^{176}Lu/^{177}Hf)_{CHUR} \times (e^{\lambda t} - 1)] - 1\}$; $T_{DM1}(Hf) = 1/\lambda \times \ln\{1 + [(^{176}Hf/^{177}Hf)_S - (^{176}Hf/^{177}Hf)_{DM}] / [(^{176}Lu/^{177}Hf)_S - (^{176}Lu/^{177}Hf)_{DM}]\}$; $T_{DM2}(Hf) = T_{DM1}(Hf) - (T_{DM1}(Hf) - t)((fcc - f_s) / (f_{cc} - f_{DM}))$, In our calculation, $fcc = -0.55$ and $f_{DM} = 0.157$.

Table 3
Major (wt%) and trace (ppm) element compositions for the late Triassic granites in the Eastern Qiangtang.

Sample	11ST-60A	11ST-60C	11ST-60E	11ST-60F	11ST-61A	11ST-61C
SiO_2	67.50	67.49	67.35	67.04	67.04	67.26
TiO_2	0.46	0.47	0.45	0.46	0.60	0.63
Al_2O_3	15.00	15.02	15.25	15.43	13.98	14.16
CaO	3.21	3.25	3.01	2.92	2.20	2.27
Fe_2O_3	4.06	4.05	3.95	3.96	4.38	4.18
K_2O	3.73	3.93	3.69	4.00	3.75	3.57
MgO	1.23	1.21	1.30	1.24	2.44	2.33
MnO	0.07	0.07	0.07	0.08	0.07	0.06
Na_2O	2.80	2.71	2.90	2.92	2.28	2.36
P_2O_5	0.12	0.12	0.12	0.12	0.18	0.18
L.O.I	1.24	1.09	1.35	1.29	2.57	2.48
Total	99.43	99.41	99.44	99.44	99.50	99.50
Mg#	38	37	40	38	53	53
A/CNK	1.04	1.03	1.07	1.07	1.18	1.19
Sc	7.64	6.57	11.4	4.58	10.8	12.6
V	35	40	51	21	66	80
Cr	15	9	23	9	80	104
Co	5	6	8	3	9	11
Ni	3	4	5	2	24	32
Ga	15.2	18.0	21.5	9.51	17.4	21.1
Rb	136	96	132	76.5	159	175
Sr	234	161	241	120	147	131
Y	26.6	23.9	28.9	16.6	27.7	36.9
Zr	201	135	162	97	170	206
Nb	12.8	13.1	14.1	6.92	14.3	15.2
Cs	2.23	2.75	3.43	1.21	3.34	2.71
Ba	1091	1020	1243	608	1137	826
La	55.9	23.3	45.1	18.1	43.8	44.6
Ce	106	48.1	85.1	35.0	89.9	89.2
Pr	11.8	5.43	9.57	4.15	10.8	10.4
Nd	42.8	20.9	33.9	15.6	41.1	39.1
Sm	7.21	4.36	6.38	3.10	7.56	7.37
Eu	1.28	0.99	1.27	0.67	1.34	1.21
Gd	6.59	4.59	5.93	3.17	6.93	6.88
Tb	0.99	0.72	0.93	0.52	0.99	1.11
Dy	5.67	4.45	5.58	3.12	5.70	6.71
Ho	1.14	0.94	1.12	0.66	1.13	1.43
Er	3.15	2.63	3.16	1.88	3.05	4.05
Tm	0.45	0.39	0.45	0.28	0.42	0.57
Yb	2.89	2.57	2.90	1.86	2.72	3.72
Lu	0.44	0.38	0.44	0.28	0.39	0.55
Hf	5.74	3.64	4.52	2.85	4.69	5.73
Ta	1.23	1.19	1.39	0.85	1.45	1.66
Pb	30.0	26.5	31.7	16.7	37.5	28.1
Th	25.4	13.6	21.4	9.69	24.4	22.9
U	3.59	2.24	3.23	1.91	2.57	3.16

A/CNK = (mol. Al_2O_3 / (CaO + K_2O + Na_2O)), Mg# = (100 × molar MgO / (MgO + FeO), FeO = 0.8998 × Fe_2O_3.

Sylvester, 1998; Clemens, 2003). The Na_2O contents (<3.2 wt.%), lower than those of I-type granites in all samples, display an affinity to S-type granite (Chappell and White, 1974, 2001), which is consistent with the classification of Chappell and White (1992) (Fig. 6c). All granite samples have similar chondrite-normalized REE patterns, showing enrichment in LREE (i.e., $(La/Yb)_{CN}$ = 6.52–13.9), with moderate negative Eu anomalies (Eu^*/Eu = 0.51–0.67, Fig. 7a). In the primitive mantle-normalized spidergram, they display conspicuous negative Nb, Ta, Sr, P, and Ti anomalies (Fig. 7b).

4.3. Whole rock Sr–Nd isotopes

The DDS granites have high and variable $^{87}Sr/^{86}Sr$ ratios (0.723624–0.741243) and low $^{143}Nd/^{144}Nd$ ratios (0.511882–0.511967) (Table 2). The initial $^{87}Sr/^{86}Sr$ ratios vary from 0.7182 to 0.7291, and ε_{Nd} (t = 220 Ma) values range from −11.09 to −10.82, different from those of the Late Triassic volcanics in the central Qiangtang (Fig. 8). Their T_{DM2} model ages are in the range of 1.87–1.90 Ga (Table 4), which are similar to those of the Precambrian metasedimentary rocks at the southern margin of Yangtze Block (Fig. 8b; Li and McCulloch, 1996).

5. Discussion

5.1. Magma origin

As described above, all the DDS granites have high A/CNK values (A/CNK > 1.0; Table 3 and Fig. 6a), and are peraluminous, which are similar to S-type granites (Fig. 6c; Chappell and White, 1974; Sylvester, 1998; Chappell and White, 2001; Clemens, 2003). The geochemical and isotopic evidence and constraints from experimental petrology have documented that most peraluminous granites originate mainly from melting of crustal rocks (e.g., Miller, 1985; Petford and Atherton, 1996; Sylvester, 1998). Their protoliths likely include aluminous-rich metasediments (metapelites), basic meta-igneous rocks (amphibolites) and quartzo-feldspathic meta-igneous rocks (orthogneisses and greywackes) in the continental crust. Clemens (2003) pointed out that metaluminous meta-igneous rocks (orthogneisses) as reported by Beard et al. (1993), and amphibolites as reported by Patiño Douce and Beard (1995) and Springer and Seck (1997), are also able to produce peraluminous felsic melts at low melting fractions and in water-deficient conditions.

All the DDS granites have higher CaO/Na_2O (0.96–1.20) and lower Al_2O_3/TiO_2 ratios (22–34) than those of the pelite-derived melts (Sylvester, 1998), suggesting that their parental magma was not the product of partial melting of just pelitic sediments. In addition, all the analyzed samples have low Rb contents (11–257 ppm; Table 1), also precluding the possibility of their formation from a pure metapelite. Experimental studies demonstrate that peraluminous melts can be produced by the dehydration melting of metaluminous basic meta-igneous rocks (amphibolites) under lower crustal conditions (e.g., Wolf and Wyllie, 1994; Patiño Douce and Beard, 1995; Springer and Seck, 1997). The melts should be high-Na, low HREE, high-Al trondhjemites in geochemical composition, with residues of garnet, clinopyroxene and amphibole (Petford and Atherton, 1996), and highly depleted in LILE, U and Th (Clemens, 2003). For the DDS granites, however, it is evident that they do not display such signatures (Table 1 and Fig. 7b). More importantly, their pronounced high initial $^{87}Sr/^{86}Sr$, and low ε_{Nd} (t = 220 Ma) and zircon $\varepsilon_{Nd}(t)$ values (Tables 2 and 4), are inconsistent with the isotopic composition of the lower crust in the Simao terrane to the south of Qiangtang terrane (Zhong, 1998). In this regard, an origin from lower crustal meta-igneous rocks for the DDS granites can be ruled

Table 4
Sr–Nd isotopic compositions of selected Dongdashan granites in the eastern Qiangtang.

	Rb	Sr	Sm	Nd	$^{87}Rb/^{86}Sr$	$^{147}Sm/^{143}Nd$	$^{87}Sr/^{86}Sr(2\sigma)$	$^{143}Nd/^{144}Nd(2\sigma)$	$^{87}Sr/^{86}Sr(t)$	$^{143}Nd/^{144}Nd(t)$	$\varepsilon_{Nd}(t)$	t_{DM}(Ga)
11ST-60C	96	161	4.36	20.9	1.73	0.13	0.723624(8)	0.511967 (10)	0.718216	0.511797	−10.89	1.88
11ST-60F	76.5	120	3.1	15.6	1.85	0.12	0.724253(10)	0.511951 (6)	0.718470	0.511794	−10.95	1.88
11ST-61A	159	147	7.56	41.1	3.14	0.11	0.736370(12)	0.511892 (8)	0.726547	0.511800	−10.82	1.87
11ST-61C	175	131	7.37	39.1	3.87	0.11	0.741243(12)	0.511882 (6)	0.729106	0.511787	−11.09	1.90

Notes: Chondrite uniform reservoir values, $^{147}Sm/^{144}Nd$ = 0.1967, $^{143}Nd/^{144}Nd$ = 0.512638, are used for the calculation. T_{DM1} values are calculated based on present-day $(^{147}Sm/^{144}Nd)_{DM}$ = 0.2137 and $(^{143}Nd/^{144}Nd)_{DM}$ = 0.51315. Sm and Nd in ppm. T_{DM1} = $1/\lambda \times \ln\{1 + [(^{143}Nd/^{144}Nd)_s - 0.51315] / [(^{147}Sm/^{144}Nd)_s - 0.2137]\}$; $T_{DM2} = T_{DM1} - (T_{DM1} - t) \times ((f_{cc} - f_s) / (f_{cc} - f_{DM}))$; Where s = sample. f_{cc}; f_s and f_{DM} are the f_{Sm} = Nd values of the continental crust, the sample and the depleted mantle, respectively. In our calculation, $f_{cc} = -0.4$ and f_{DM} = 0.08592; where t = the Formation age of the rock.

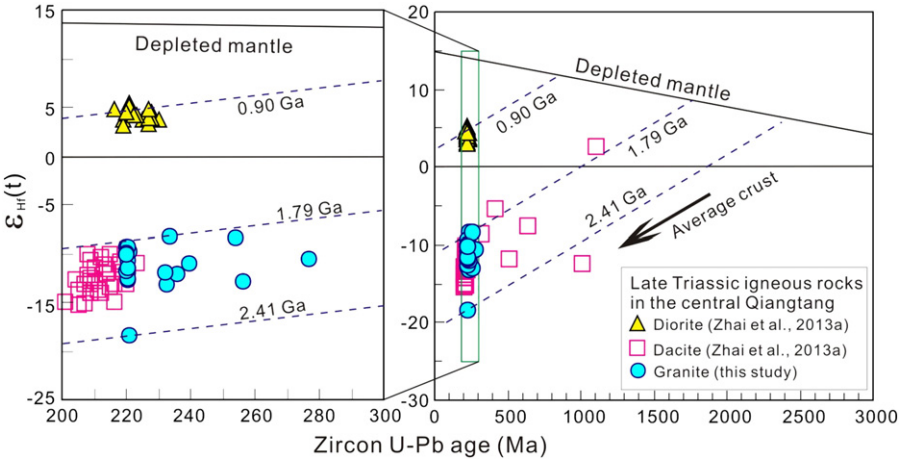

Fig. 5. Relationship between $\varepsilon_{Hf}(t)$ values and U–Pb ages for zircons from the intrusive rocks in the Yidun terrane. Hf isotopic compositions of chondrite and depleted mantle are from Blichert-Toft and Albarede (1997) and Vervoort and Blichert-Toft (1999).

out. Also, the heat-flow models do not support the proposal that most granitic rocks originate from partial melting of the lower crust, as concluded by Clemens (2003).

Interaction of basaltic magmas with Al-rich metasedimentary rocks has also been advocated to generate peraluminous granites (Sylvester, 1998; Sandeman and Clark, 2003). However, the Sr–Nd isotopic data of the DDS granites clearly show that a direct and significant involvement of mantle magmas is unlikely in their genesis. Consequently, their major element signatures, such as high CaO/Na_2O and low Al_2O_3/TiO_2 ratios (Fig. 9a), coupled with their whole-rock Sr–Nd and zircon Hf isotopic compositions, more likely indicate their derivation from a greywacke or psammite source (Miller, 1985; Holtz and Johannes, 1991; Clemens, 2003). In the Rb/Ba vs. Rb/Sr diagram (Fig. 9b), most of the DDS granitic rocks plot close to the greywacke that has a clay-poor source (Chappell and White, 1992; Sylvester, 1998), although some do plot near the shale, indicating a mixed source dominated by greywacke, but including minor shale.

Considering the old $T_{DM2}(Nd)$ and $T_{DM2}(Hf)$ model ages (1.87–1.90 Ga and 1.79–2.41 Ga, respectively) of the DDS granites, we propose that the metasedimentary source was in the middle/upper crust, likely corresponding to metasedimentary rocks of the Precambrain Ningduo and Caoqu groups in the Eastern Qiangtang (You et al., 2001). Especially, the Ningduo and Caoqu group metasediments that are composed of metagreywackes, metapelite and minor interlayered metabasalts (You et al., 2001), are the most feasible source for the generation of the DDS granitic magma. The relatively flat HREE patterns of all the DDS granites (Fig. 7a), with $(Gd/Yb)_N$ values in the range of 1.12 to 1.40, further suggest an absence of garnet in the source and, therefore, middle/upper crustal levels of partial melting. This feature is common to many peraluminous granites (e.g., Rossi et al., 2002). In addition, the strongly negative Eu, Ba, Nb, Tb, Sr, P and Ti anomalies (Fig. 7a and b) suggest that these peraluminous magmas have undergone some degrees of fractional crystallization during magmatic evolution.

5.2. Tectonic setting

As discussed above, the identification of the Carboniferous ophiolites within the QMB in the central Qiangtang suggests that the Paleo-Tethys Ocean was located between the Eastern and Western Qiangtang terranes during the late Paleozoic (Li and Zheng, 1993; Li et al., 2006; Zhai et al., 2013c). Also, the recognition of the Permo-Early Triassic arc igneous rocks (Yang et al., 2011) in the central Qiangtang further demonstrates that the subduction of oceanic crust developed until the Early Triassic. However, the tectonic setting responsible for the Middle–Late Triassic HP metamorphic event and magmatism has long been disputed. Some workers suggest an arc regime to account for the Middle–Late Triassic metamorphic thermal event and magmatism (Liu et al., 2011; Zhai et al., 2011, 2013a). In contrast, other researchers have invoked a continental rift to explain the characteristics of the Late Triassic magmatism and sedimentation, and believed that the subduction of oceanic crust and subsequent continent–continent collision had been completed by the Middle Triassic (Fu et al., 2008; Wang et al., 2008; Fu et al., 2010).

Although the presence of adakitic rocks (i.e., diorites from the Baohu area and some volcanic rocks from the Juhuashan area) led Zhai et al. (2013a) to believe that a Late Triassic subduction-related arc regime is responsible for the HP metamorphism and magmatism, the identification of the HP lawsonite-like eclogite (Zhai et al., 2011) and blueschists (Liu et al., 2011) does not support a hot subduction that is necessary for producing adakitic melts in the area, but argues for a cold subduction at that time (e.g., Ravna et al., 2010). Moreover, the recognition of the Carboniferous (345–357 Ma) ophiolite in the area, including oceanic cumulate, gabbro, basalt, actinolitite and plagiogranite (Zhai et al., 2013c), also argues against a young (<25 Ma), hot oceanic subduction that is requisite for the generation of the Late Triassic (~220 Ma) adakitic rocks. Accordingly, the generation of adakitic rocks could be the results of re-melting of the detached oceanic slab in a post-collisional environment (also see the discussion in Section 5.4). In fact, the following several lines of evidence lend strong support to a post-collisional setting responsible for the Late Triassic tectono-magmatism and sedimentation in the central Qiangtang block, rather than a subduction-related arc environment (Zhai et al., 2011, 2013a).

Firstly, in the case of the Late Triassic sedimentation, the onset of the Late Triassic continental molasse formation that mainly includes alluvial and fluvial sedimentary facies associated with continental volcanic explosion facies (Wang et al., 2000; Li et al., 2003; Wang et al., 2004) in the Mesozoic Qiangtang basin, marks the end of oceanic subduction and the initiation of a continental rift-related extension in the early Late Triassic. Moreover, the basal conglomerates of the Nadi Kangri Formation (the volcanic rocks from this formation were dated at the range of 225–205 Ma; Wang et al., 2007; Zhai and Li, 2007; Wang et al., 2008) are poorly rounded, some of which contain the eclogite gravels and blueschist fragments that were derived from underlying beds (Fu et al., 2010). This also implies that these HP metamorphic rocks had been rolled back or exhumed back to the surface by ~225 Ma. Secondly, the synchronous development of the Late Triassic volcanic rocks in the two sides of the QMB or the Longmu Co–Busu suture belt, along with the fact that they share broad geochemical similarities (Fu et al., 2010), indicates that they probably erupted in the same tectonic environment. In this respect, an island arc regime is difficult to account for such a pattern of magmatism. On the Rb vs. Y + Nb and Hf–Rb/30-Ta × 3 diagrams (Fig. 10a and b), all the granites fall within the post-

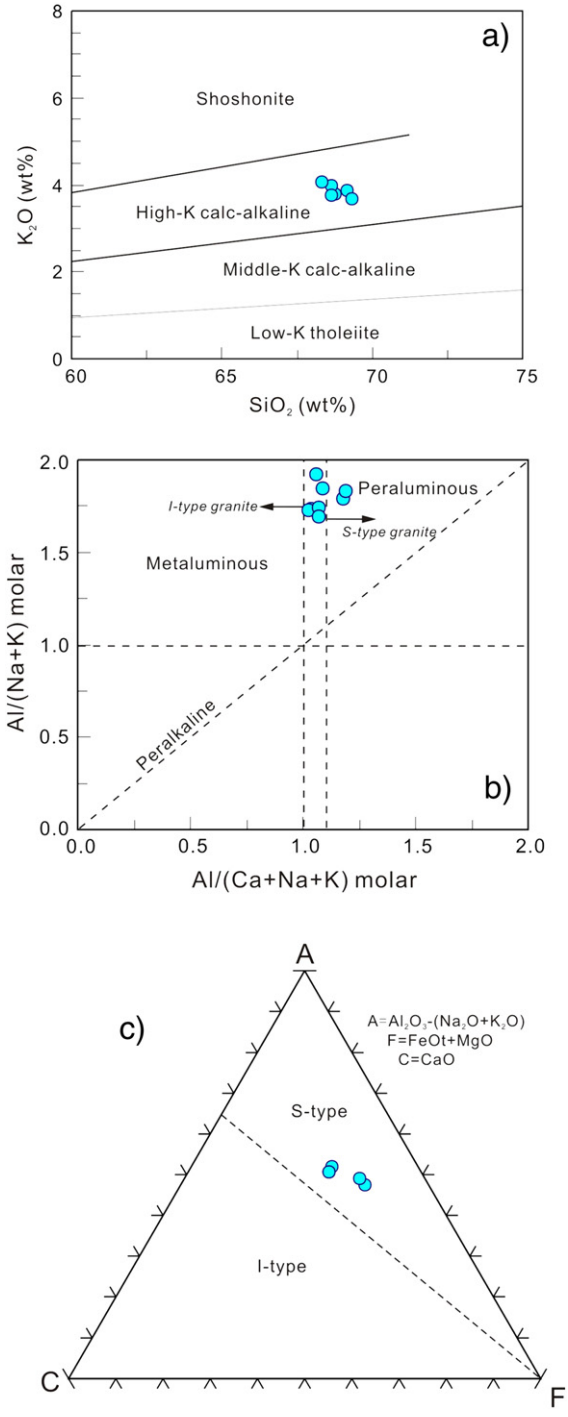

Fig. 6. (a) K_2O versus SiO_2 (after Winchester and Floyd, 1977), (b) molar Al/(K + Na) versus Al/(Ca + Na + K) diagram, and (c) ACF diagram (after Chappell and White, 1992). Whole rock compositions are corrected for loss-on-ignition.

collision or late-collision fields and not the syn-collision or volcanic arc fields, which further supports the above interpretation. More importantly, the Late Triassic igneous rocks show a bimodal affinity that is a typical rock association of extension-related magmatism (Zhang et al., 2011). Furthermore, the basic volcanic rocks have an affinity to the within-plate basalt in geochemical composition (Fu et al., 2010), rather than the subduction-related island arc basalt.

Taken together, a post-collisional environment is the most feasible explanation for the development of tectono-magmatism in the central Qiangtang and the sedimentation in the Mesozoic Qiangtang basin during the Late Triassic. This also implies that the Paleo-Tethys Ocean had not been closed until the earliest Triassic, and that the peak collision between the Gondwana-derived Western Qiangtang terrane and the Eastern Qiangtang terrane with a Cathysian affinity had been completed at least by the early Late Triassic (~237 Ma) (Zhai et al., 2011).

5.3. Geodynamic model

It has been established that several tectonic scenarios are responsible for post-collisional extension, including (1) convective thinning of the lithosphere (e.g., Houseman and Molnar, 1997), (2) lithospheric delamination (e.g., Kay and Kay, 1993), (3) gravitational or orogenic collapse (e.g., Turner et al., 1999; Rey et al., 2001), and (4) slab detachment or breakoff (e.g., Davies and von Blanckenburg, 1995). These mechanisms have the potential to cause upwelling of the asthenosphere that would perturb the original thermal gradient and lead to lithospheric extension and large volumes of magma generation (Bonin, 2004).

However, taking into account the presence of eclogites and blueschists in the central Qiangtang terrane (Liu et al., 2011; Zhai et al., 2011), it is quite clear that the former three scenarios are difficult to lead to the exhumation of these HP–UHP metamorphic rocks from a depth of >70 km (a peak condition of eclogite facies metamorphism at 410–460 °C and 2.0–2.5 GPa, Zhai et al., 2011). On the contrary, slab breakoff is the most effective mechanism to trigger the HP and UHP metamorphic rocks to roll back and exhume back to the surface (Von Blanckenburg and Davies, 1995). Moreover, slab breakoff generally results in a narrow linear zone of magmatism, uplift that propagates along strike and moderate amounts of erosional products in intramontane basins (von Blanckenburg and Davies, 1995). Such scenario is the most viable to explain the distribution patterns of Late Triassic magmatism and sedimentation in the central Qiangtang (Fig. 1b).

For instance, the mid-Triassic igneous rocks form a linear belt that is parallel to the HP metamorphic belt in the central Qiangtang (Fig. 1b; XZBGM, 1993). The association of the exhumed HP rocks with igneous rocks is diagnostic of the breakoff process (Davies and von Blanckenburg, 1995), which is akin to the features described from other orogenic belts, such as the Alps (von Blanckenburg and Davies, 1995; Marchant and Stampfli, 1997) and the Basin and Range Province (Camp et al., 2003), particularly the Aegean islands of Greece, with the exposure of both a blueschist belt and granitoids (Schliestedt et al., 1987).

In this scenario, following slab breakoff, a detached part of the lithosphere would sink into the mantle and force some mantle material down with it. Hot asthenosphere would rise and heat the mantle directly above the descending slab as it sinks deeper. Heat from the asthenospheric mantle would be transferred to the mantle lithosphere by conduction, and this would trigger partial melting of the overlying enriched wedge mantle (Davies and von Blanckenburg, 1995). The basaltic magmas formed by this melting would rise into the crust, where they further induce large-scale crustal melting, resulting in granitic or rhyolitic magmatism (Davies and von Blanckenburg, 1995; Atherton and Ghani, 2002). Owing to the thickened nature of the crust, magmatism would be dominated by felsic rocks, with only minor basic magmas at this stage in the central Qiangtang (e.g., Wang et al., 2007; Fu et al., 2008; Wang et al., 2008; Fu et al., 2010; Zhang et al., 2011; Zhai et al., 2013a). Also, following slab breakoff, buoyancy forces triggered the subducted slab to retreat (Jolivet and Faccenna, 2000) and drove the HP–UHP metamorphic rocks upward along the subduction zone from ~75 km depth to the surface. Subsequent further uplift of continental crust would result in partial erosion of HP–UHP rocks into the foreland basin, coeval with the emplacement of igneous rocks (von Blanckenburg and Davies, 1995). Hence, this scenario accounts for the exhumation of HP eclogites and blueschists within the QMB and their occurrence in the Qiangtang basin (Pullen et al., 2008; Liu et al., 2011; Zhai et al., 2011). Meanwhile, the detached oceanic slab would also melt due to being surrounded by the hot asthenosphere. Such melt shows an adakitic affinity, such as the Late Triassic diorites

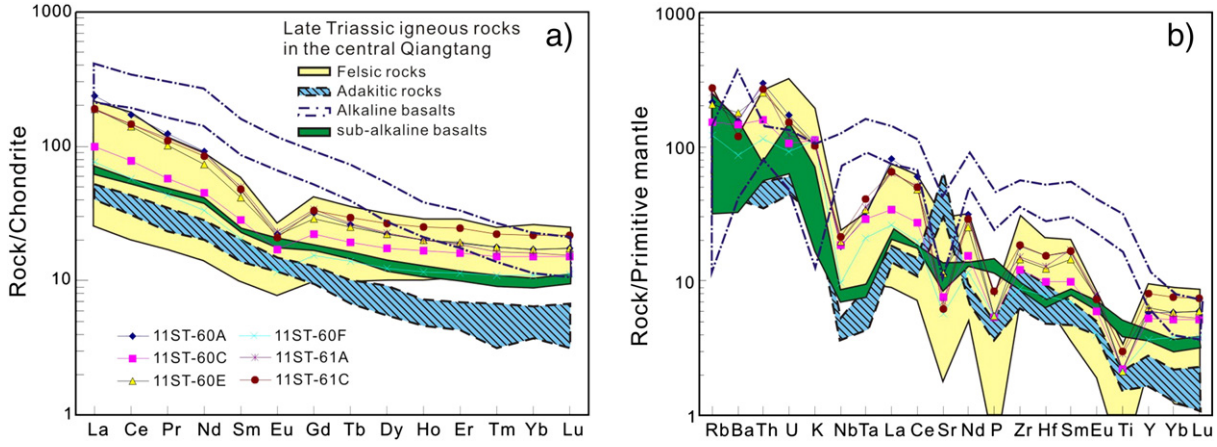

Fig. 7. (a) Chondrite-normalized REE patterns and (b) primitive mantle-normalized spider diagrams for the DDS granites. Normalizing values of chondrite and primitive mantle are from Taylor and McLennan (1985) and Sun and McDonough (1989), respectively. The Late Triassic felsic rocks are from Fu et al. (2010), Zhang et al. (2011) and Zhai et al. (2013a). The sub-alkaline and alkaline basalts are from Fu et al. (2010) and Zhang et al. (2011), respectively. The adakitic rocks are from Zhai et al. (2013a).

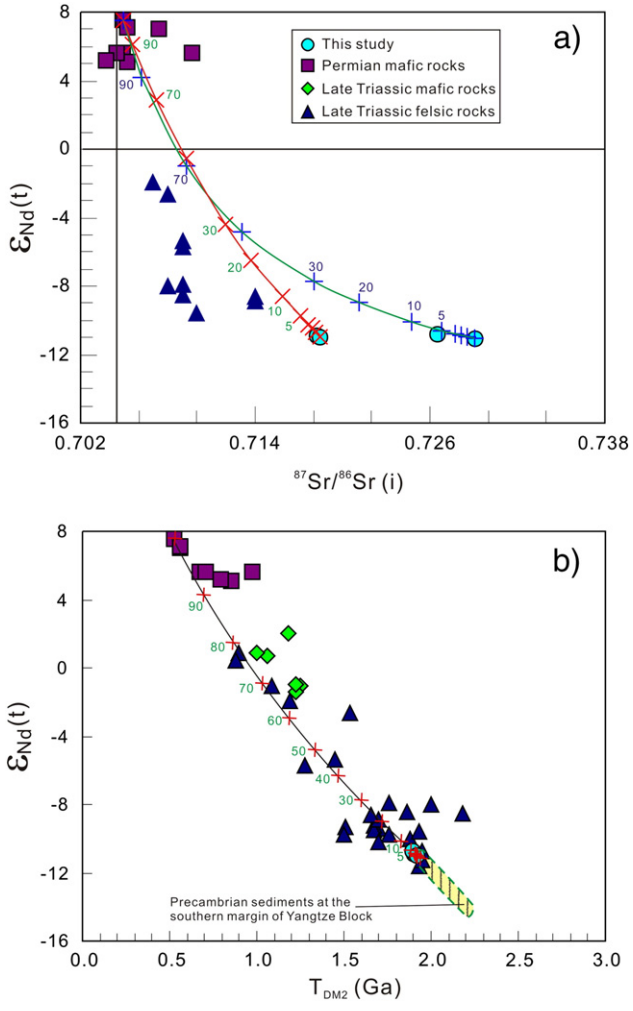

Fig. 8. $\varepsilon_{Nd}(t)$ versus (a) $^{87}Sr/^{86}Sr(t)$ ($t = 220$ Ma) and (b) T_{DM2}. Precambrian sediments at the southern margin of Yangtze Block are from Li and McCulloch (1996); permian mafic rocks are from Zhai et al. (2013b); Late Triassic mafics are from Zhang et al. (2011); Late Triassic felsic rocks are from Zhang et al. (2011) and Zhai et al. (2013a). The curve representing the mixing proportion between two components, i.e., mantle-derived magma and middle/upper crustal melts corresponding to the mafic rocks are from Zhai et al. (2013b) and the DDS granitic magma from this study, respectively.

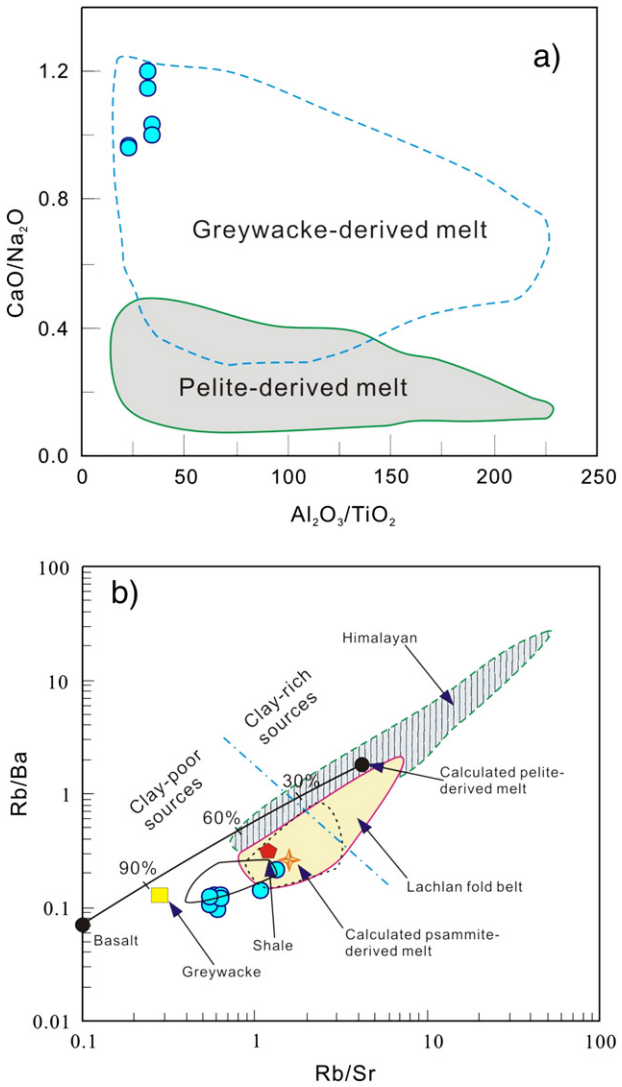

Fig. 9. (a) CaO/Na_2O versus Al_2O_3/TiO_2 (after Jung and Pfander, 2007) and (b) Rb/Ba versus Rb/Sr diagrams. Fields of the Himalayan and Lachlan fold belt peraluminous granites are from Patiño Douce and Harris (1998) and Sylvester (1998), respectively.

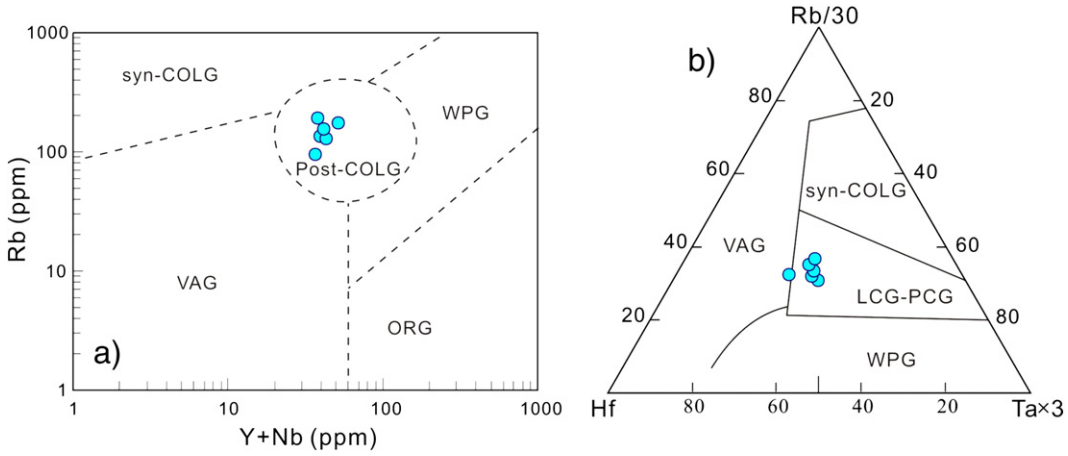

Fig. 10. Geochemical discrimination diagrams of (a) Rb versus Y + Nb of Pearce (1996) and (b) Rb–Hf–Ta of Harris et al. (1986) for the DDS granites. Abbreviations: VAG, volcanic arc granites; ORG, ocean ridge granites; WPG, within-plate granites; syn-COLG and post-COLG, syn- and post-collision granites; LCG-PCG, late- and post-collision granites.

in the Baohua area and volcanic rocks in the Juhuashan area (Zhai et al., 2013a).

5.4. Geochronological framework of Mesozoic tectono-magmatism and its implications

In recent years, a large number of precise chronological data have been reported for Mesozoic metamorphism-related thermal and magmatic events from the central Qiangtang area. The metamorphic thermal records include the garnet Lu–Hf ages of 244 ± 11 Ma for the epidote eclogite and 223.4 ± 4.5 Ma for the garnet glaucophane in the Gemo area (Pullen et al., 2008), the zircon U–Pb ages of 230 ± 3 Ma and 237 ± 4 Ma for two eclogite samples (Zhai et al., 2011), the $^{40}Ar/^{39}Ar$ ages of 223 ± 4 Ma and 227 ± 4 Ma of sodic amphiboles from the Qiangtang blueschists (Zhai et al., 2009), the $^{40}Ar/^{39}Ar$ ages of 203 to 222 Ma for white mica from metapelite (Kapp et al., 2000, 2003; Zhai et al., 2009), and the phengite $^{40}Ar/^{39}Ar$ ages of 223–211 Ma for the eclogite and garnet-phengite schist (Zhai et al., 2011; Liang et al., 2012). In the case of the Triassic magmatism, a large volume of Late Triassic igneous rocks have also been verified, along with minor Early Triassic arc granites (Yang et al., 2011) and Middle Triassic alkaline diabases (Zhang et al., 2011) in the central Qiangtang. For example, the Nadi Kangri volcanic rocks erupted in the Geladaindong (220.4 ± 2.3 Ma, Fu et al., 2010), Juhua Mountain (225 ± 1 Ma and 219 ± 4 Ma, Zhai and Li, 2007; Fu et al., 2008), Jiangai (210 ± 2 Ma, Zhai et al., 2013a), Guoganjianian (215 ± 3 Ma, Zhai et al., 2013a), and the Nadigangri, Shishui River and Woruo Mountain (210 ± 4 Ma, 208 ± 4 Ma and 216 ± 4 Ma, respectively, Wang et al., 2007) areas; the volcanic rocks from the Wanghuling Formation (comparable to the Nadi Kangri Formation) in the Mayer Gangri region of the central Qiangtang give SHRIMP zircon U–Pb ages of 214 ± 4 Ma and 215 ± 3 Ma (Li et al., 2007). Also, the dioritic and granitic magmatism developed in the Baohua (223 ± 2 Ma, Zhai et al., 2013a) and the Dongdala areas (220 ± 2 Ma, this study).

Taking into account the fact that zircon crystals (dated at 230 ± 4 Ma and 237 ± 4 Ma) from the Qiangtang eclogite contain numerous inclusions of the HP eclogite facies assemblages, including garnet, omphacite and phengite that are similar to those in the matrix of eclogite (Zhai et al., 2011), this likely indicates that the HP–UHP peak metamorphism had been completed before the formation of zircon crystals, at least by ~237 Ma. Moreover, the presence of the alkaline diabase with an age of 234 ± 4 Ma in the Tuohepingco area, central Qiangtang (Zhang et al., 2011) also indicates that the subducted slab had been broken off and subsequent decompressional melting of upwelling asthenosphere had taken place at that time, coinciding with this inference. Therefore, the garnet Lu–Hf isochron age of 244 ± 11 Ma probably represents the peak time of HP–UHP metamorphism (Pullen et al., 2008), and the age range of 237–203 Ma should record the post-peak retrograde and magmatism-related thermal events.

Alternatively, the occurrence of the HP metamorphic fragments in the lowest segment of the Late Triassic strata with an oldest depositional age at 225 ± 1 Ma (based on the dating result of the Nadi Kangri volcanic rock, Fu et al., 2008) implies that the HP–UHP rocks had been rolled back to the surface at least at ~225 Ma and were rapidly eroded into the Mesozoic Qiangtang basin. According to Ernst's conclusion that the interval of formation and exhumation of the UHP rocks worldwide is not larger than 15 Ma (Ernst, 2006), it is possible that the HP–UHP rocks might have been exhumed at ~230 Ma in the central Qiangtang. Considering the fact that the emplacement time of 234 ± 4 Ma for the alkaline diabases (Zhang et al., 2011) is synchronous with the magmatic zircon age of 237 ± 4 Ma from eclogite sample (Zhai et al., 2011) within errors, it likely indicates that the slab break-off event might have started at ~237 Ma, shortly after the peak metamorphism in central Qiangtang, resulting in rapid exhumation of the central Qiangtang HP–UHP rocks. In this case, the exhumation rates of the HP–UHP rocks may be up to ~5 mm/year. Such speedy unloading appears to be greater than currently measured uplift and erosion rates in the Himalayas (Searle, 1996), but is roughly compatible with exhumation rates of ~4 mm/year calculated by Genser et al. (1996) for the Eastern Alps. A simplified model for the evolution of the Paleo-Tethys in the central Qiangtang during Permian to Late Triassic times was shown in Fig. 11.

6. Conclusions

Geochronological and geochemical data for the Late Triassic Dongdashan (DDS) granites in the Eastern Qiangtang terrane, Eastern Tibetan plateau, coupled with previously published results, allow us to reach the following conclusions:

1) The DDS batholith was emplaced in the Late Triassic (at 220.3 ± 0.7 Ma).
2) Geochemically, the DDS granites display peraluminous affinities with negative zircon $\varepsilon_{Hf}(t)$ values and old depleted Hf model ages, suggesting that they originated from partial melting of Paleoproterozoic crustal basement.
3) Continent–continent collision (between the Eastern and Western Qiangtang) of the Paleo-Tethys occurred by the Early Triassic, and the HP–UHP peak metamorphism ended by the Mid-Triassic of ~237 Ma.
4) A post-collisional tectonic setting related to slab breakoff was responsible for the Mesozoic magmatism and the exhumation of high-pressure eclogites and blueschist.

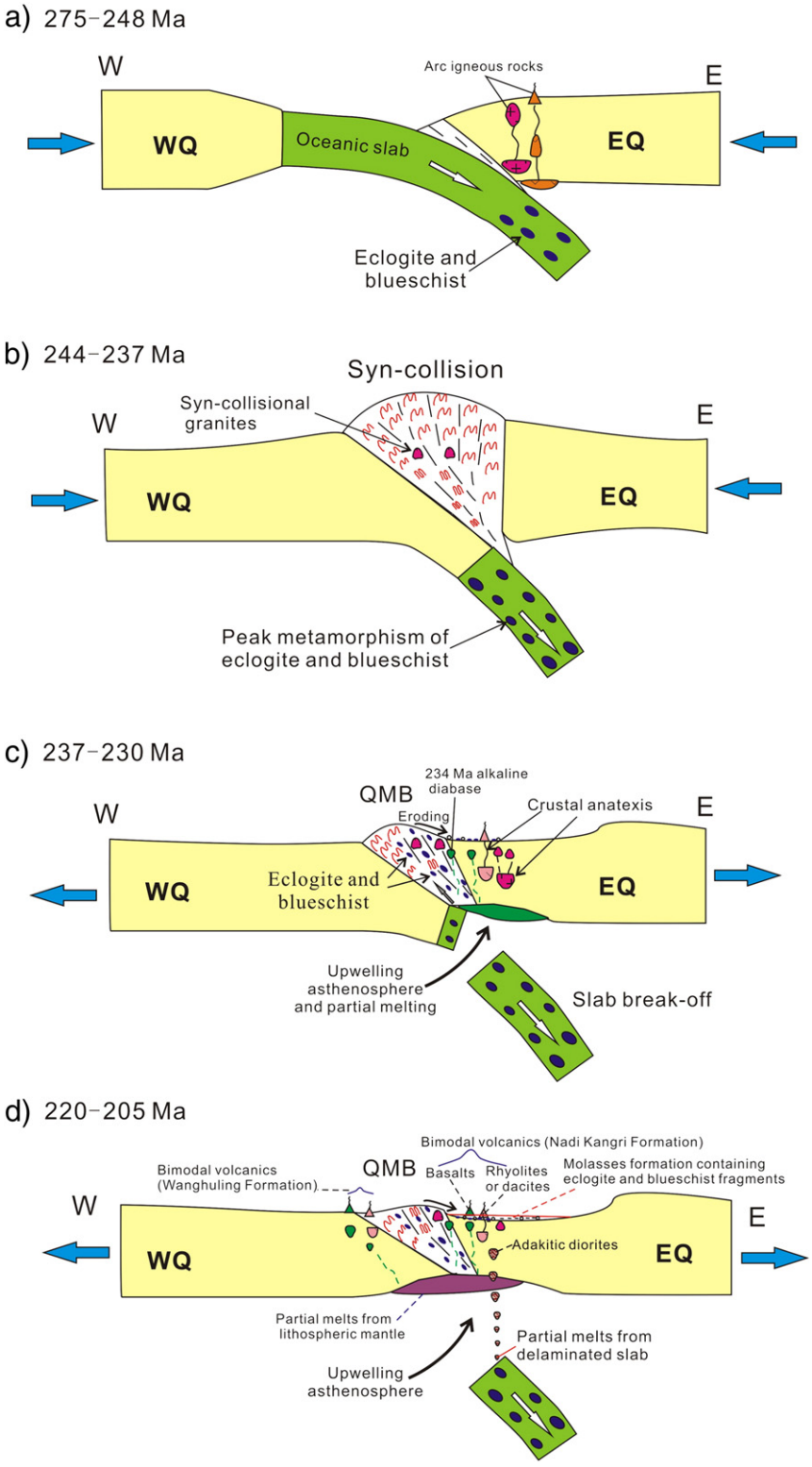

Fig. 11. Schematic models for (a) oceanic subduction, (b) syn-collisional orogen and peak metamorphism of eclogite and blueschist, (c) break-off of the Paleo-Tethyan slab and (d) post-collisional magmatism in the central Qiangtang area. WQ: the Western Qiangtang; EQ: the Eastern Qiangtang; QMB: the Qiangtang metamorphic belt.

Acknowledgments

We acknowledge Y.-F. Cai for his assistance during LA-ICP-MS dating and zircon Hf analyses, respectively. Constructive reviews by chief editor M. Santosh, associate editor Zeming Zhang and two reviewers (Marian Munteanu and one anonymous reviewer) are also gratefully acknowledged. This research was supported by the National Basic Research Program of China (2014CB440901) and the Natural Science Foundation of China (Grant nos. 40972046, 41190073, 41172095 and 41272126). This is a contribution from the Guangzhou Institute of Geochemistry, Chinese Academy of Sciences (GIG, CAS; No. 1824).

References

Anderson, T., 2002. Correction of common lead in U–Pb analyses that do not report ^{204}Pb. Chemical Geology 192, 59–79.

Atherton, M.P., Ghani, A.A., 2002. Slab breakoff: a model for Caledonian, Late Granite syn-collisional magmatism in the orthotectonic (metamorphic) zone of Scotland and Donegal, Ireland. Lithos 62, 65–85.

Barbarin, B., 1999. A review of the relationships between granitoid types, their origins and their geodynamic environments. Lithos 46, 605–626.

Beard, J.S., Abirz, R.J., Lofgren, G.E., 1993. Experimental melting of crustal xenoliths from Kilbourne Hole, New Mexco and implications for the contamination and genesis of magmas. Contributions to Mineralogy and Petrology 115, 88–102.

Blichert-Toft, J., Albarede, F., 1997. The Lu–Hf geochemistry of chondrites and the evolution of the mantle–crust system. Earth and Planetary Science Letters 148, 243–258.

Bonin, B., 2004. Do coeval mafic and felsic magmas in post-collisional to within-plate regimes necessarily imply two contrasting, mantle and crustal, sources? A review. Lithos 78, 1–24.

Bonin, B., 2007. A-type granites and related rocks: evolution of a concept, problems and prospects. Lithos 97, 1–29.

Brown, M., 1994. The generation, segregation, ascent and emplacement of granite magma: the migmatite-to-crustally-derived granite connection in thickened orogens. Earth-Science Reviews 36, 83–130.

Camp, V.E., Ross, M.E., Hanson, W.E., 2003. Genesis of flood basalts and Basin and Range volcanic rocks from Steens Mountain to the Malheur River Gorge, Oregon. Geological Society of America Bulletin 115, 105–128.

Chappell, B.W., White, A.J.R., 1974. Two contrasting granite types. Pacific Geology 8, 173–179.

Chappell, B.W., White, A.J.R., 1992. I- and S-type granites in Lachlan Fold Belt. Transactions of the Royal Society of Edinburgh 83, 1–26.

Chappell, B.W., White, A.J.R., 2001. Two contrasting granite types: 25 years later. Australian Journal of Earth Sciences 48, 488–489.

Chen, J.L., Xu, J.F., Wang, B.D., Kang, Z.Q., Li, J., 2010. Origin of Cenozoic alkaline potassic volcanic rocks at KonglongXiang, Lhasa terrane, Tibetan Plateau: products of partial melting of a mafic lower-crustal source? Chemical Geology 273, 286–299.

Ciancaleoni, L., Marquer, D., 2004. Syn-extension leucogranite deformation during convergence in the Eastern Central Alps: example of the Novate intrusion. Terra Nova 18, 170–180.

Clemens, J.D., 2003. S-type granitic magmas—petrogenetic issues, models and evidence. Earth-Science Reviews 61, 1–18.

Condie, K.C., Kröner, A., 2013. The building blocks of continental crust: evidence for a major change in the tectonic setting of continental growth at the end of the Archean. Gondwana Research 23, 394–402.

Davies, J.H., von Blanckenburg, F., 1995. Slab breakoff: a model of lithosphere detachment and its test in the magmatism and deformation of collisional orogens. Earth and Planetary Science Letters 129, 85–102.

Deng, J., Wang, C.M., Li, G.J., 2012. Style and process of the superimposed mineralization in the Sanjiang Tethys. Acta Petrologica Sinica 28, 1349–1361 (in Chinese with English abstract).

Eby, G.N., 1992. Chemical subdivision of the A-type granitoids: petrogenetic and tectonic implications. Geology 20, 641–644.

Ernst, W.G., 2006. Preservation/exhumation of ultrahigh-pressure subduction complexes. Lithos 92, 321–335.

Fu, X.G., Wang, J., Wang, Z.J., Chen, W.X., 2008. U–Pb zircon age and geochemical characteristics of volcanic rocks from the Juhua mountain area in the northern Qiangtang basin, northern Xizang (Tibet). Geological Review 54, 232–242 (in Chinese with English abstract).

Fu, X.G., Wang, J., Tan, F.W., Chen, M., Chen, W.B., 2010. The Late Triassic rift-related volcanic rocks from Eastern Qiangtang, northern Tibet (China): age and tectonic implications. Gondwana Research 17, 135–144.

Gaillard, F., Scaillet, B., Pichavant, M., 2004. Evidence for present day leucogranite pluton growth in Tibet. Geology 32, 801–804.

Genser, J., van Wees, J.D., Cloetingh, S., Neubauer, F., 1996. Eastern Alpine tectono-metamorphic evolution: Constraints from two-dimensional P-T-t modeling. Tectonics 15. http://dx.doi.org/10.1029/95TC03289.

Griffin, W.L., Pearson, N.J., Elusive, E., Jackson, S.E., van Achtenberg, E., O'Reilly, S.Y., She, S.R., 2000. The Hf isotope composition of carbonic mantle: LAM-MC-ICPMS analysis of zircon megacrysts in kimberlites. Geochimica et Cosmochimica Acta 64, 133–147.

Griffin, W.L., Belousova, E.A., Shee, S.R., Pearson, N.J., O'Reilly, S.Y., 2004. Archean crustal evolution in the northern Yilgam Craton: U–Pb and Hf-isotope evidence from detrital zircons. Precambrian Research 131, 231–282.

Harris, N.B.W., Marzouki, F.M.H., Ali, S., 1986. The Jabel Sayid complex, Arabian shield: geochemical constraints on the origin of peralkaline and related granites. Journal of the Geological Society, London 143, 287–295.

Harrison, T.M., Grove, M., Lovera, O.M., Catlos, E.J., 1998. A model for the origin of Himalayan anatexis and inverted metamorphism. Journal of Geophysical Research 103, 27,017–27,032.

Holtz, F., Johannes, W., 1991. Genesis of peraluminous granites: I. Experimental investigation of melt composition at 3 and 5 kb and various H_2O activities. Journal of Petrology 32, 909–934.

Hou, Z.Q., Yang, Y.Q., Wang, H.P., Qu, X.M., Lü, Q.T., Huang, D.H., Wu, X.Z., Tang, S.H., Zhao, J.H., 2003. Collision-Orogenic Progress and Mineralization System of Yidun Arc. Geological Publishing House, Beijing (345 pp. (in Chinese)).

Hou, Z.Q., Zaw, K., Pan, G.T., Mo, X.X., Xu, Q., Hu, Y.Z., Li, X.Z., 2007. Sanjiang Tethyan metallogenesis in SW China: tectonic setting, metallogenic epochs and deposit types. Ore Geology Reviews 31, 48–87.

Hou, Z.Q., Zhang, H.R., Pan, X.F., Yang, Z.M., 2011. Porphyry Cu (−Mo−Au) deposits related to melting of thickened mafic lower crust—examples from the eastern Tethyan metallogenic domain. Ore Geology Reviews 39, 21–45.

Houseman, G.A., Molnar, P., 1997. Gravitational (Rayleigh–Taylor) instability of a layer with non-linear viscosity and convective thinning of continental lithosphere. Geophysical Journal International 128, 125–150.

Jolivet, L., Faccenna, C., 2000. Mediterranean extension and the Africa–Eurasia collision. Tectonics 19, 1095–1106.

Jung, S., Pfander, F.J.A., 2007. Source composition and melting temperatures of orogenic granitoids: constraints from CaO/Na_2O, Al_2O_3/TiO_2 and accessory mineral saturation thermometry. European Journal of Mineralogy 19, 859–870.

Kapp, P., Yin, A., Manning, C.E., Murphy, M., Harrison, T.M., Spurlin, M., Ding, L., Deng, X.G., Wu, C.M., 2000. Blueschist-bearing metamorphic core complexes in the Qiangtang block reveal deep crustal structure of northern Tibet. Geology 28, 19–22.

Kapp, P., Yin, A., Manning, C.E., Harrison, T.M., Taylor, M.H., Ding, L., 2003. Tectonic evolution of the early Mesozoic blueschist-bearing Qiangtang metamorphic belt, central Tibet. Tectonics 22, 1043. http://dx.doi.org/10.1029/2002TC001383.

Kay, R.W., Kay, M.S., 1993. Delamination and delamination magmatism. Tectonophysics 219, 177–189.

Li, X.H., McCulloch, M.T., 1996. Nd isotopic evolution of sediments from the southern margin of the Yangtze Block and its tectonic significance. Acta Petrologica Sinica 12 (3), 359–369 (in Chinese with English abstract).

Li, C., Zheng, A., 1993. Paleozoic stratigraphy in the Qiangtang region of Tibet: relations of the Gondwana and Yangtze continents and ocean closure near the end of the Carboniferous. International Geology Review 35, 797–804.

Li, Y., Wang, C.S., Yi, H.S., 2003. The Late Triassic collision and sedimentary responses at western segment of Jinshan River Suture, Tibet. Acta Sedimentologica Sinica 21, 191–197 (in Chinese with English abstract).

Li, X.H., Liu, D.Y., Sun, M., Li, W.X., Liang, X.R., Liu, Y., 2004. Precise Sm–Nd and U–Pb isotopic dating of the super-giant Shizhuyuan polymetallic deposit and its host granite, Southeast China. Geological Magazine 141, 225–231.

Li, C., Zhai, Q.G., Dong, Y.S., Huang, X.P., 2006. Discovery of eclogite and its geological significance in Qiangtang area, central Tibet. Chinese Science Bulletin 51, 1095–1100.

Li, C., Zhai, Q.G., Dong, Y.S., Yu, J.J., Huang, X.P., 2007. Establishment of the Upper Triassic Wanghuling Formation at Guoganjianian Mountain, central Qiangtan, Qinghai–Tibet plateau, and its significance. Geological Bulletin of China 26, 1003–1008 (in Chinese with English abstract).

Liang, H.Y., Sun, W.D., Su, W.C., Zartman, R.E., 2009. Porphyry copper–gold mineralization at Yulong, China, promoted by decreasing redox potential during magnetite alteration. Economic Geology 104, 587–596.

Liang, X., Wang, G.H., Yuan, G.L., Liu, Y., 2012. Structural sequence and geochronology of the Qomo Ri accretionary complex, Central Qiangtang, Tibet: implications for the Late Triassic subduction of the Paleo-Tethys Ocean. Gondwana Research 22, 470–481.

Liu, Y.S., Hu, Z.C., Zong, K.Q., Zong, K.Q., Gao, C.G., Gao, S., Xu, J., Chen, H.H., 2010. Reappraisement and refinement of zircon U–Pb isotope and trace element analyses by LA-ICP-MS. Chinese Science Bulletin 55 (15), 1535–1546.

Liu, Y., Santosh, M., Zhao, Z.B., Niu, W.C., Wang, G.H., 2011. Evidence for palaeo-Tethyan oceanic subduction within central Qiangtang, northern Tibet. Lithos 127, 39–53.

Ludwig, K.R., 2003. User's Manual for Isoplot 3.00 a Geochronological Toolkit for Microsoft Excel.

Lv, B.X., Wang, Z., Zhang, N.D., Duan, J.Z., 1993. Granitoid in the Sanjiang Region (Nujiang–Lancangjiang–Jinsha Jiang Region) and Their Metallogenic Specialization. Geological Publishing House, Beijing 1–108 (in Chinese with English abstract).

Marchant, R.H., Stampfli, G.M., 1997. Subduction of continental crust in the Western Alps. Tectonophysics 269, 217–235.

Martin, H., 1987. Petrogenesis of Archean trondhjemites, tonalites and granodiorites from eastern Finland: major and trace element geochemistry. Journal of Petrology 28, 921–953.

Metcalfe, I., 2013. Gondwana dispersion and Asian accretion: tectonic and palaeogeographic evolution of eastern Tethys. Journal of Asian Earth Sciences 66, 1–33.

Miller, C.F., 1985. Are strongly peraluminous magmas derived from pelitic sedimentary sources? Journal of Geology 93, 673–689.

Miller, C.F., McDowell, S.M., Mapes, R.W., 2003. Hot and cold granites? Implications of zircon saturation temperatures and preservation of inheritance. Geology 31, 529–532.

Moyen, J.-F., Martin, H., Jayananda, M., 2001. Multi-element geochemical modelling of crust–mantle interactions during late-Archaean crustal growth: the Closepet granite (South India). Precambrian Research 112, 87–105.

Pan, G.T., Xu, Q., Hou, Z.Q., Wang, L.Q., Du, D.X., Mo, X.X., Li, D.M., Wang, M.J., LI, X.Z., Jiang, X.S., Hu, Y.Z., 2003. Archipelagic Orogenesis, Metallogenic Systems and Assessment of the Mineral Resources along the Nujiang–Lancangjiang–Jinshajiang Area in Southwestern China. Geological Publishing House, Beijing (420 pp. (in Chinese with English abstract)).

Pan, G., Ding, J., Yao, D., Wang, L., compilers, 2004. Guidebook of 1:1 500 000 geologic map of the Qinghai-Xizang (Tibet) plateau and adjacent areas: Chengdu, China, Chengdu Cartographic Publishing House, 48 pp. (in Chinese).

Patiño Douce, A.E., Beard, J.S., 1995. Dehydration-melting of biotite gneiss and quartz amphibolite from 3 to 15 kbar. Journal of Petrology 36, 707–738.

Patiño Douce, A.E., Harris, N., 1998. Experimental constraints on Himalayan anatexis. Journal of Petrology 39, 689–710.

Pearce, J.A., 1996. Sources and settings of granitic rocks. Episodes 19, 120–125.

Pearce, J.A., Harris, N.B.W., Tindle, A.G., 1984. Trace element discrimination diagrams for the tectonic interpretation of granitic rocks. Journal of Petrology 25, 956–983.

Peng, T.P., Wilde, S.A., Wang, Y.J., Fan, W.M., Peng, B.X., 2013. Mid-Triassic felsic igneous rocks from the southern Lancangjiang Zone, SW China: petrogenesis and implications for the evolution of Paleo-Tethys. Lithos 168–169, 15–32.

Petford, N., Atherton, M., 1996. Na-rich partial melts from newly underplated basaltic crust: the Cordillera Blanca Batholith, Peru. Journal of Petrology 37, 1491–1521.
Pitcher, W., 1983. Granite types and tectonic environment. In: Hsu, K. (Ed.), Mountain Building Processes. Academic Press, London, pp. 19–40.
Press, W.H., Flannery, B.P., Teukolsky, S.S., Vetterling, W.T., 1986. Numerical Recipes. Cambridge University Press, Cambridge 818.
Pullen, A., Kapp, P., Gehrels, G.E., Vervoort, J.D., Ding, L., 2008. Triassic continental subduction in central Tibet and Mediterranean-style closure of the Paleo-Tethys Ocean. Geology 36, 351–354.
Pullen, A., Kapp, P., Gehrels, G.E., Ding, L., Zhang, Q., 2011. Metamorphic rocks in central Tibet: lateral variations and implications for crustal structure. Geological Society of America Bulletin 123, 585–600.
Qi, L., Hu, J., Gregoire, D.C., 2000. Determination of trace elements in granites by inductively coupled plasma–mass spectrometry. Talanta 51, 507–513.
Ravna, E.J.K., Andersen, T.B., Jolivet, L., Capitani, C.D.E., 2010. Cold subduction and the formation of lawsonite eclogite—constraints from prograde evolution of eclogitized pillow lava from Corsica. Journal of Metamorphic Geology 28, 381–395.
Rey, P., Vanderhaeghe, O., Teyssier, C., 2001. Gravitational collapse of the continental crust: definitions, regimes, mechanisms and modes. Tectonophysics 342, 435–449.
Rossi, J.N., Toselli, A.J., Saavedra, J., Sial, A.N., Pellitero, E., Ferreira, V.P., 2002. Common crustal sources for contrasting peraluminous facies in the early Paleozoic Capillitas Batholith, NW Argentina. Gondwana Research 5, 325–337.
Sandeman, H.A., Clark, A.H., 2003. Glass-rich, cordierite–biotite rhyodacite, Valle Ninahuisa, Puno, southeastern Peru: petrological evidence for hybridization of 'Lachlan S-type' and potassic mafic magmas. Journal of Petrology 44, 355–385.
Scherer, E., Munker, C., Mezger, K., 2001. Calibration of the lutetium–hafnium clock. Science 293, 683–687.
Schliestedt, M., Altherr, R., Matthews, A., 1987. Evolution of the Cycladic Crystalline Complex: petrology, isotope geochemistry and geochronology. In: Helgeson, H.C. (Ed.), Chemical Transport in Metasomatic Processes. Reidel, Dordrecht, pp. 389–428.
Searle, M.P., 1996. Cooling history, erosion, exhumation, and kinetics of the Himalaya–Karakorum–Tibet orogenic belt. In: Yin, A., Harrison, T.M. (Eds.), The Tectonic Evolution of Asia. Cambridge University Press, New York, pp. 110–137.
Shi, J.R., Dong, Y.S., Wang, S.Y., 2009. Dating and tectonic significance of plagiogranite from Guoganjianian Mountain, central Qiangtang, northern Tibet, China. Geological Bulletin of China 28 (9), 1236–1243 (in Chinese with English abstract).
Springer, W., Seck, H.A., 1997. Partial fusion of basic granulites at 5 to15 kbar: implications for the origin of TTG magmas. Contributions to Mineralogy and Petrology 127, 30–45.
Steiger, R.H., Jäger, E., 1997. Subcommission on geochronology: convection or the use of decay constants in geo- and cosmo-chronology. Earth and Planetary Science Letters 36, 359–362.
Streckeisen, A., 1967. Classification and nomenclature of igneous rocks. Final report of an inquiry. Neues Jahrbuch für Mineralogie Abhandlungen 107, 144–204.
Sun, S.S., McDonough, W.F., 1989. Chemical and isotopic systematics of oceanic basalts: implications for mantle composition and processes. In: Saunders, A.D., Norry, M.J. (Eds.), Magmatism in the ocean basins. Geological Society, London, Special Publications, vol. 42, pp. 313–345.
Sylvester, P.J., 1989. Post-collisional alkaline granites. Journal of Geology 97, 261–280.
Sylvester, P.J., 1998. Postcollisional strongly peraluminous granites. Lithos 45, 29–44.
Taylor, S.R., McLennan, S.M., 1985. The Continental Crust: Its Composition and Evolution. Blackwell, Oxford Press (312 pp.).
Turner, S.P., Platt, J.P., George, R.M.M., Kelley, S.P., Pearson, D.G., Nowell, G.M., 1999. Magmatism associated with orogenic collapse of the Betic–Alboran domain, SE Spain. Journal of Petrology 40, 1011–1036.
Vervoort, J.D., Blichert-Toft, J., 1999. Evolution of the depleted mantle; Hf isotope evidence from juvenile rocks through time. Geochimica et Cosmochimica Acta 63, 533–556.
von Blanckenburg, F., Davies, J.H., 1995. Slab breakoff—a model for syncollisional magmatism and tectonics in the Alps. Tectonics 14, 120–131.
Wang, X.F., Metcalfe, I., Jian, P., He, L.Q., Wang, C.S., 2000. The Jinshajiang–Ailaoshan suture zone, China: tectonostratigraphy, age and evolution. Journal of Asian Earth Sciences 18, 675–690.
Wang, L.Q., Li, D.M., Guan, S.P., Xu, T.R., 2001. The evolution of the Luchun–Hongponiuchang superimposed rifting basin, Deqin County, Yunan Province. Journal of Mineral Petrology 21, 81–89 (in Chinese with English abstract).
Wang, J., Tan, F.W., Li, Y.L., Li, Y.T., Chen, M., Wang, C.S., Guo, Z.J., Wang, X.L., Du, B.W., Zhu, Z.F., 2004. The Potential of the Oil and Gas Resources in Major Sedimentary Basins on the Qinghai–Xizang Plateau. Geological Publishing House, Beijing pp. 34–88 (in Chinese with English abstract).
Wang, J., Wang, Z.J., Chen, W.X., Fu, X.G., 2007. New evidences for the age assignment of the Nadi Kangri Formation in the North Qiangtang depression, northern Tibet, China. Geological Bulletin of China 26, 404–409 (in Chinese with English abstract).
Wang, J., Fu, X., Chen, W., Wang, Z., Tan, F., Chen, M., Zhuo, J., 2008. Chronology and geochemistry of the volcanic rocks in Woruo Mountain region, northern Qiangtang depression: implications to the Late Triassic volcanic–sedimentary events. Science in China Series D: Earth Sciences 51, 194–205.
Wang, Y.J., Zhang, A.M., Fan, W.M., Peng, T.P., Zhang, F.F., Zhang, Y.H., Bi, X.W., 2010. Petrogenesis of late Triassic post-collisional basaltic rocks of the Lancangjiang tectonic zone, southwest China, and tectonic implications for the evolution of the eastern Paleotethys: geochronological and geochemical constraints. Lithos 120 (3–4), 529–546.
Wang, B.Q., Zhou, M.F., Li, J.W., Yan, D.P., 2011. Late Triassic porphyritic intrusions and associated volcanic rocks from the Shangri-La region, Yidun terrane, Eastern Tibetan Plateau: Adakitic magmatism and porphyry copper mineralization. Lithos 127, 24–38.
Wang, C.M., Deng, J., Carranza, E.J.M., Santosh, M., 2014. Tin metallogenesis associated with granitoids in the southwestern Sanjiang Tethyan Domain: nature, deposit types, and tectonic setting. Gondwana Research 26, 576–593.
Wedepohl, K.H., 1991. Chemical composition and fractionation of the continental crust. Geologische Rundschau 80, 207–223.
Winchester, J.A., Floyd, P.A., 1977. Geochemical discrimination of different magma series and their differentiation products using immobile elements. Chemical Geology 20, 325–343.
Wolf, M.B., Wyllie, P.J., 1994. Dehydration melting of amphibolite at 10 kbar: the effects of temperature and time. Contributions to Mineralogy and Petrology 115, 369–383.
Woodhead, J.D., Hergt, J.M., Shelley, M., Eggins, S., Kemp, R., 2004. Zircon Hf-isotope analysis with an excimer laser, depth profiling, ablation of complex geometries, and concomitant age estimation. Chemical Geology 209, 121–135.
Xia, X.P., Sun, M., Zhao, G.C., Wang, Y.J., 2011. Quasi-simultaneous determination of U–Pb and Hf isotope compositions of zircon by excimer laser-ablation multiple-collector ICPMS. Journal of Analytical Atomic Spectrometry 26, 1868–1871.
XZBGM (Bureau of Geology and Mineral Resources of Xizang Autonomous Region), 1993. Regional Geology of Xizang (Tibet) Autonomous Region. Geological Publishing House, Beijing (in Chinese with English abstract).
Yang, T.N., Zhang, H.R., Liu, Y.X., Wang, Z.L., Song, Y.C., Yang, Z.S., Tian, S.H., Xie, H.Q., Hou, K.J., 2011. Permo-Triassic arc magmatism in central Tibet: evidence from zircon U–Pb geochronology, Hf isotopes, rare earth elements, and bulk geochemistry. Chemical Geology 284, 270–282.
Yang, X.A., Liu, J.J., Cao, Y., Han, S.Y., Gao, B.Y., Wang, H., Liu, Y.D., 2012. Geochemistry and S, Pb isotope of the Yangla copper deposit, western Yunnan, China: implication for ore genesis. Lithos 144–145, 231–240.
You, Z.P., Chen, Y.L., Zang, K.Z., 2001. Relationship between the Ningduo and the Qangsum and the Caoqu groups of the Precambrian system in east Tibet. Tibet Geology 19, 39–42 (in Chinese with English abstract).
Zhai, Q.G., Li, C., 2007. Zircon SHRIMP dating of volcanic rock from Nadigangri Formation in Juhuashan, Qiangtang, Northern Tibet and its geological significance. Acta Geologica Sinica 81, 795–800 (in Chinese with English abstract).
Zhai, Q.G., Li, C., Huang, X.P., 2007. The fragment of Paleo-Tethys ophiolite from central Qiangtang, Tibet: geochemical evidence of metabasites in Guoganjianian. Science in China Series D-Earth Sciences 50, 1302–1309.
Zhai, Q.G., Li, C., Wang, J., Chen, W., Zhang, Y., 2009. Petrology, mineralogy and $^{40}Ar/^{39}Ar$ chronology for Rongma blueschist from central Qiangtang, northern Tibet. Acta Petrologica Sinica 25, 2281–2288 (in Chinese with English abstract).
Zhai, Q.G., Zhang, R.Y., Jahn, B.M., Li, C., Song, S.G., Wang, J., 2011. Triassic eclogites from central Qiangtang, northern Tibet, China: petrology, geochronology and metamorphic P–T path. Lithos 125, 173–189.
Zhai, Q.G., Jahn, B.M., Su, L., Ernst, R.E., Wang, K.L., Zhang, R.Y., Wang, J., Tang, S.H., 2013a. SHRIMP zircon U–Pb geochronology, geochemistry and Sr–Nd–Hf isotopic compositions of a mafic dyke swarm in the Qiangtang terrane, northern Tibet and geodynamic implications. Lithos 174, 28–43.
Zhai, Q.G., Jahn, B.M., Su, L., Wang, J., Mo, X.X., Lee, H.Y., Wang, K.L., Tang, S., 2013b. Triassic arc magmatism in the Qiangtang area, northern Tibet: Zircon U–Pb ages, geochemical and Sr–Nd–Hf isotopic characteristics, and tectonic implications. Journal of Asian Earth Sciences 63, 162–178.
Zhai, Q.G., Jahn, B.M., Wang, J., Su, L., Mo, X.X., Wang, K.L., Tang, S.H., Lee, H.Y., 2013c. The Carboniferous ophiolite in the middle of the Qiangtang terrane, Northern Tibet: SHRIMP U–Pb dating, geochemical and Sr–Nd–Hf isotopic characteristics. Lithos 168–169, 186–199.
Zhang, Z.M., Santosh, M., 2012. Tectonic evolution of Tibet and surrounding regions. Gondwana Research 21, 1–3.
Zhang, K.J., Tang, X.C., 2009. Eclogites in the interior of the Tibetan Plateau and their geodynamic implications. Chinese Science Bulletin 54, 2556–2567.
Zhang, K.J., Xia, B.D., Liang, X.W., 2002. Mesozoic and Paleogene sedimentary facies and paleogeography of Tibet: tectonic implications. Geological Journal 37, 217–246.
Zhang, K.J., Cai, J.X., Zhang, Y.X., Zhao, T.P., 2006a. Eclogites from central Qiangtang, northern Tibet (China) and tectonic implications. Earth and Planetary Science Letters 245, 722–729.
Zhang, K.J., Zhang, Y.X., Li, B., Zhu, Y.T., Wei, R.Z., 2006b. The blueschist-bearing Qiangtang metamorphic belt (northern Tibet, China) as an in situ suture zone: evidence from geochemical comparison with the Jinsa suture. Geology 34, 493–496.
Zhang, K.J., Zhang, Y.X., Xia, B.D., He, Y.B., 2006c. Temporal variations of the Mesozoic sandstone composition in the Qiangtang block, northern Tibet (China): implications for provenance and tectonic setting. Journal of Sedimentary Research 76, 1035–1048.
Zhang, K.J., Zhang, Y.X., Tang, X.C., Xie, Y.W., Sha, S.L., Peng, X.J., 2008. First report of eclogites from central Tibet, China: evidence for ultra-deep continental subduction prior to the Cenozoic India–Asian collision. Terra Nova 20, 302–308.
Zhang, X.R., Shi, R.D., Huang, Q.S., Liu, D.L., Cidan, S.L., Yang, J.S., Ding, L., 2010. Finding of high-pressure mafic granulites in the Amdo basement, central Tibet. Chinese Science Bulletin 55, 3694–3702.
Zhang, K.J., Tang, X.C., Wang, Y., Zhang, Y.X., 2011. Geochronology, geochemistry, and Nd isotopes of early Mesozoic bimodal volcanismin northern Tibet, western China: constraints on the exhumation of the central Qiangtang metamorphic belt. Lithos 121, 167–175.
Zhang, K.J., Zhang, Y.X., Tang, X.C., Xia, B.D., 2012. Late Mesozoic tectonic evolution and growth of the Tibetan plateau prior to the Indo-Asian collision. Earth-Science Reviews 114, 236–249.

Zhang, Z.M., Dong, X., Santosh, M., Zhao, G.C., 2014. Metamorphism and tectonic evolution of the Lhasa terrane, Central Tibet. Gondwana Research 25, 170–189.
Zheng, Y.F., Xiao, W.J., Zhao, G.C., 2013. Introduction to tectonics of China. Gondwana Research 23, 1189–1206.
Zhong, D.L., 1998. The Paleotethys orogenic belt in west of Sichuan and Yunnan. Science Publishing House, Beijing 1–230 (in Chinese).
Zhu, D.C., Zhao, Z.D., Niu, Y.L., Mo, X.X., Chung, S.L., Hou, Z.Q., Wang, L.Q., Wu, F.Y., 2011. The Lhasa Terrane: record of a microcontinent and its histories of drift and growth. Earth and Planetary Science Letters 301, 241–255.
Zhu, D.C., Zhao, Z.D., Niu, Y.L., Dilek, Y., Hou, Z.Q., Mo, X.X., 2013. The origin and pre-Cenozoic evolution of the Tibetan Plateau. Gondwana Research 23, 1429–1454.